

# Catalytic oxidation of ammonia: A pre-occupied-anchoring-site strategy for enlarging Ag nanoparticles at low Ag loading and achieving enhanced activity and selectivity on Ag-CuO<sub>x</sub>/Al<sub>2</sub>O<sub>3</sub> catalyst

Zhao Li <sup>a,1</sup>, Fei Wang <sup>a,b,\*1</sup>, Fudong Liu <sup>c,\*\*</sup>, Shaohua Xie <sup>c</sup>, Changbin Zhang <sup>d,f</sup>, Ping Ning <sup>a,b</sup>, Kai Li <sup>a,b,\*</sup>, Hong He <sup>d,e,f</sup>, Xiao Cheng Zeng <sup>g,\*\*</sup>

<sup>a</sup> Faculty of Environmental Science and Engineering, Kunming University of Science and Technology, Kunming 650500, China

<sup>b</sup> National-Regional Engineering Center for Recovery of Waste Gases from Metallurgical and Chemical Industries, Kunming 650500, China

<sup>c</sup> Department of Civil, Environmental, and Construction Engineering, Catalysis Cluster for Renewable Energy and Chemical Transformations (REACT), NanoScience Technology Center (NSTC), University of Central Florida, Orlando, FL 32816, United States

<sup>d</sup> State Key Joint Laboratory of Environment Simulation and Pollution Control, Research Center for Eco-Environmental Sciences, Chinese Academy of Sciences, Beijing 100085, China

<sup>e</sup> Center for Excellence in Regional Atmospheric Environment, Institute of Urban Environment, Chinese Academy of Sciences, Xiamen 361021, China

<sup>f</sup> University of Chinese Academy of Sciences, Beijing 100049, China

<sup>g</sup> Department of Materials Science & Engineering, City University of Hong Kong, Kowloon 999077, Hong Kong, SAR China



## ARTICLE INFO

### Keywords:

Ag nanoparticles  
Anchoring sites  
Pre-occupy  
Anchoring mechanism  
NH<sub>3</sub>-SCO

## ABSTRACT

The Ag nanoparticles (Ag<sub>NPs</sub>) in Ag/Al<sub>2</sub>O<sub>3</sub> catalysts play a crucial role in the selective catalytic oxidation of NH<sub>3</sub> (NH<sub>3</sub>-SCO). To enhance NH<sub>3</sub>-SCO activity, Cu, which has stronger anchoring ability than Ag, is introduced onto Al<sub>2</sub>O<sub>3</sub>, reducing available anchoring sites for Ag. As Ag cannot displace anchored Cu species, Ag species agglomerate into larger Ag<sub>NPs</sub> even with low Ag loading. Consequently, these enlarged Ag<sub>NPs</sub> become more active centers for NH<sub>3</sub>-SCO. The optimal Ag:Cu molar ratio is confirmed as 2:3. This 'pre-occupied-anchoring-site' strategy decreases Ag loading to 1/5 of the original, reducing catalyst costs while maintaining activity. *In situ* diffuse reflectance infrared Fourier-transform spectroscopy (DRIFTS) studies reveal that NH<sub>3</sub>-SCO on 2Ag1.8Cu/Al (weight ratio) catalyst follows the hydrazine mechanism below 200 °C, coexisting with the imide mechanism from 200–250 °C, and solely the imide mechanism beyond 250 °C. This strategy is applicable to various transition metals, including Mn, Co, Ni, and Fe, promoting cost-effective Ag<sub>NPs</sub> formation.

## 1. Introduction

Ammonia (NH<sub>3</sub>) has been confirmed to play a crucial role in the formation of haze pollution, and gaseous NH<sub>3</sub> can damage the human respiratory tract and plant leaf stomata [1,2]. NH<sub>3</sub> in the atmosphere mainly comes from the spontaneous production in nature and human activities. Anthropogenic sources mainly include animal husbandry, agriculture, industry and transportation [3–5]. Moreover, with the increasingly stringent NO<sub>x</sub> emission standards implemented around the world, under the large-scale application of deNO<sub>x</sub> technologies such as selective catalytic reduction (SCR) and selective non-catalytic reduction (SNCR), the aggravation of NH<sub>3</sub> slip problems is inevitable [6,7].

Therefore, the development of efficient and inexpensive NH<sub>3</sub> purification technology is receiving increasing attention in both academia and industry.

At present, selective catalytic oxidation of NH<sub>3</sub> (NH<sub>3</sub>-SCO) to N<sub>2</sub> and H<sub>2</sub>O is the most effective NH<sub>3</sub> purification technology. Catalysts with precious metals as active components such as Pt, Pd, Rh, Au, Ir display high NH<sub>3</sub>-SCO performance [8–17]. Although most transition metal-based catalysts (such as Cu, Fe, Co and Mn etc.) also have certain NH<sub>3</sub>-SCO catalytic activity, they are not suitable for NH<sub>3</sub> removal from stationary sources and indoor air due to their inferior performance at low temperatures [18–24]. Ag-based catalysts have been widely studied in NH<sub>3</sub>-SCO due to their broad operation temperature window and

\* Corresponding authors at: Faculty of Environmental Science and Engineering, Kunming University of Science and Technology, Kunming 650500, China.

\*\* Corresponding authors.

E-mail addresses: wangfei@kust.edu.cn (F. Wang), fudong.liu@ucf.edu (F. Liu), likaikmust@163.com (K. Li), xzeng26@cityu.edu.hk (X.C. Zeng).

<sup>1</sup> These authors contributed equally to this work.

relatively low cost [25–28]. Our previous studies showed that Ag nanoparticles ( $\text{Ag}_{\text{NPs}}$ ) are the intrinsic active centers for  $\text{NH}_3\text{-SCO}$  reaction [29]. The  $\text{H}_2$  reduction pretreatment and increasing the Ag loading (usually up to 10 wt%) are common methods to improve the  $\text{NH}_3\text{-SCO}$  performance of Ag-based catalysts [29–31]. However, on one hand, the high-temperature reduction pretreatment using  $\text{H}_2$  has potential safety hazards and also increases the energy consumption. Meanwhile, the  $\text{Ag}_{\text{NPs}}$  formed by agglomerating the Ag species in  $\text{H}_2$  at high temperatures are easily redispersed in oxygen-rich atmosphere, making it difficult to maintain high catalytic stability [32]. On the other hand, increasing Ag loading to improve the  $\text{NH}_3\text{-SCO}$  activity will increase the catalyst production cost considerably. In addition, the  $\text{N}_2$  selectivity in  $\text{NH}_3\text{-SCO}$  on pure Ag-based catalysts is usually low, which is an obvious drawback that needs improvement. To resolve these issues, Ag–Cu dual site catalysts have been developed with remarkable success in the  $\text{NH}_3\text{-SCO}$  reaction [26,33], with higher catalytic activity and  $\text{N}_2$  selectivity than single-component catalysts. However, the performance of these catalysts remains suboptimal, necessitating operation under reaction conditions characterized by a gas hourly space velocity (GHSV) below 30,000  $\text{h}^{-1}$  and a reaction temperature exceeding 270 °C to achieve 100%  $\text{NH}_3$  conversion. Furthermore, the catalytic stability of these high-loading Ag–Cu catalysts remains untested for practical applications.

In our previous work, it has been reported that the terminal hydroxyl groups on  $\gamma\text{-Al}_2\text{O}_3$  are the anchoring sites for Ag atoms [34]. Therefore, the abundant terminal hydroxyl groups on  $\text{Al}_2\text{O}_3$  support are favorable for the dispersion of Ag as single atoms, while the Ag species tend to agglomerate to form Ag clusters and  $\text{Ag}_{\text{NPs}}$  when the terminal hydroxyl groups are insufficient for Ag anchoring. The abundant  $\text{Ag}_{\text{NPs}}$  in Ag-based catalysts are beneficial to the substantial improvement of catalytic performance in  $\text{NH}_3\text{-SCO}$  reaction. However, obtaining high-concentration  $\text{Ag}_{\text{NPs}}$  on  $\text{Al}_2\text{O}_3$  often requires more Ag loaded, which leads to an increase in the catalyst cost. In this study, we propose a ‘pre-occupied-anchoring-site’ strategy using Cu, an inexpensive transition metal with higher anchoring strength to  $\text{Al}_2\text{O}_3$ , to occupy the anchoring sites on  $\text{Al}_2\text{O}_3$  surface in advance. Thus, Ag can be forced to agglomerate into  $\text{Ag}_{\text{NPs}}$  due to the lack of anchoring sites, and the conversion rate of  $\text{NH}_3$  can be greatly improved. Meanwhile, as an effective promoter, Cu addition can significantly improve the  $\text{N}_2$  selectivity as well, and finally improve the overall catalytic performance in the  $\text{NH}_3\text{-SCO}$  reaction. Additionally, the ‘pre-occupied-anchoring-site’ strategy proves to be universal, as observed with Co, Fe, Mn, and Ni, forcing Ag species to agglomerate into  $\text{Ag}_{\text{NPs}}$  and consequently enhancing  $\text{NH}_3\text{-SCO}$  performance.

## 2. Materials and methods

### 2.1. Catalyst preparation

The catalysts were prepared using the wet impregnation method. Initially, 5 g of  $\gamma\text{-Al}_2\text{O}_3$  was mixed with deionized water to create a suspension under stirring. Subsequently, an aqueous solution containing 0.1 g of Ag and varying amounts of X metal (where X represents Cu, Co, Mn, Fe, and Ni) was added to the suspension in the form of an aqueous nitrate solution. After 3 h of impregnation, the mixture was dried using a vacuum rotary evaporator. Further, the samples were dried at 105 °C for 12 h and calcined in air at 550 °C for 3 h. Finally, the catalysts were sieved to 40–60 mesh and given specific names, such as  $2\text{Ag}_x\text{X}/\text{Al}$ , where 2 indicates 2 wt% loading of Ag, x denotes the loading of X metal, and Al denotes  $\text{Al}_2\text{O}_3$ . If no Ag or X was added, the samples were referred to as  $x\text{X}/\text{Al}$  or  $2\text{Ag}/\text{Al}$ . For example, in the  $2\text{Ag}1.5\text{Cu}/\text{Al}$  and  $2\text{Ag}1.6\text{Co}/\text{Al}$  samples, the Ag loading was 2 wt% and the molar ratio of Ag:Cu and Ag:Co was 2:3. The  $2\text{Ag}/\text{Al}$  and  $1.2\text{ Cu}/\text{Al}$  reference catalysts were also prepared and both had the same metal loading in moles as  $9.26 \times 10^{-4}$  mol/5 g support. The catalysts, which were subjected to pretreatment with 10 vol%  $\text{H}_2/\text{N}_2$  for 2 h at different temperatures, were named

$2\text{Ag-T}/\text{Al}$  and  $1.2\text{Cu-T}/\text{Al}$ , where T represents the pretreatment temperature.

Based on the aforementioned preparation, an appropriate quantity of synthesized  $2\text{Ag}/\text{Al}$  or  $x\text{Cu}/\text{Al}$  was mixed with deionized water, forming a suspension. Next, an aqueous solution of  $\text{Cu}(\text{NO}_3)_2$  or  $\text{AgNO}_3$  was added to achieve a loading of x wt% Cu or 2 wt% Ag, respectively. Following the impregnation for 3 h, the mixture was dried using a vacuum rotary evaporator. Subsequently, the samples were dried at 105 °C for 12 h and calcined in air at 550 °C for 3 h. The resulting samples were named  $x\text{Cu}/2\text{Ag}/\text{Al}$  or  $2\text{Ag}/x\text{Cu}/\text{Al}$ , respectively.

### 2.2. Sample characterization

A Thermo Nicolet iS-50 equipped with an MCT/A detector was used to perform *in situ* diffuse reflectance infrared Fourier transform spectroscopy (DRIFTS) to measure the change in anchoring sites for Ag or Cu species and to study the  $\text{NH}_3\text{-SCO}$  reaction mechanism. The sample was pretreated before measurement with 20 vol%  $\text{O}_2/\text{N}_2$  at 500 °C for 30 min. In typical experiments, 500 ppm  $\text{NH}_3$  or a mixture of 500 ppm  $\text{NH}_3 + 10$  vol%  $\text{O}_2$  at a total flow rate of 300  $\text{mL}\cdot\text{min}^{-1}$  was introduced into the DRIFTS cell. All spectra were recorded at 800–4000  $\text{cm}^{-1}$  by accumulating 100 scans with a resolution of 4  $\text{cm}^{-1}$ .

*In situ* Fourier transform infrared spectroscopy (FTIR) experiments in the transmission mode were also conducted on a Thermo Nicolet iS-50 with a high-vacuum chamber (base pressure of  $< 5 \times 10^{-8}$  mbar).

Powder X-ray diffraction (XRD) measurements were performed on a computerized PANalytical Empyrean diffractometer with a Cu K $\alpha$  radiation source.

Transmission electron microscopy (TEM), scanning transmission electron microscopy (STEM), and energy-dispersive X-ray spectroscopy (EDS) for elemental mapping were conducted on an FEI talosF200s. The Ag dispersion was calculated based on the average Ag particle size from the STEM images.

Diffuse reflectance ultraviolet-visible (UV-vis) spectra were measured at room temperature in the air using  $\text{BaSO}_4$  as a reference (U-3100 UV-vis spectrophotometer, Hitachi Co., Japan). All UV-vis spectra were collected at 190–800 nm with a resolution of 1 nm.

*In situ* Raman spectra were obtained using a Renishaw in Via Raman Spectrometer equipped with an *in situ* reaction chamber. The excitation source was an air-cooled 633-nm laser with an output power of 150 mW.

Ag K-edge X-ray absorption fine structure (XAFS) spectra, including X-ray absorption near edge structure (XANES) and extended X-ray absorption fine structure (EXAFS), were recorded in the fluorescence mode at room temperature using Beamline 7-BM QAS of the National Synchrotron Light Source II (NSLS-II), Brookhaven National Laboratory. Cu K-edge XAFS spectra, including XANES and EXAFS, were collected in fluorescence mode at the BL14W beamline of the Shanghai Synchrotron Radiation Facility. Data were analyzed using Athena and Artemis from the Demeter software package. The filtered  $k^2$  weighted  $\chi(k)$  was Fourier-transformed into R-space with a  $k$  range of 2–12  $\text{\AA}^{-1}$ .

$\text{H}_2$  temperature-programmed reduction ( $\text{H}_2\text{-TPR}$ ) experiments were performed using a Micromeritics AutoChem II 2920 apparatus. All samples were pretreated at 500 °C for 30 min under 20 vol%  $\text{O}_2/\text{Ar}$  and then cooled to 50 °C, followed by Ar purging for 20 min. Further, the  $\text{H}_2\text{-TPR}$  profiles were obtained by passing a flow of 10 vol%  $\text{H}_2/\text{Ar}$  through the sample from 50 °C to 800 °C (with a ramping rate of 5 °C/min).  $\text{H}_2$  consumption was continuously monitored using a thermal conductivity detector.

### 2.3. Density functional theory (DFT) calculations

The anchoring strength of Ag and Cu atoms on the hydroxylated  $\gamma\text{-Al}_2\text{O}_3$  surface was calculated using the density functional theory (DFT) method in the formalism of the Perdew–Burke–Ernzerhof (PBE) functional [35] with the van der Waals correction proposed by Stefan Grimme (i.e., DFT-D3 method) [36], as implemented in the Vienna ab

initio simulation package (VASP 5.4.4) [37]. The projector augmented wave (PAW) method was used to describe the core-valence electron interaction [38], and a cutoff energy of 400 eV was adopted during the calculations. Based on our previous research [39], a  $(2 \times 2)$  supercell of the hydroxylated  $\gamma\text{-Al}_2\text{O}_3$  (100) surface was modeled. The top two layers and the adsorbents were fully relaxed, while the bottom layers were fixed to mimic the bulk region. To avoid the periodic image interaction normal to the surface, a vacuum gap of 20 Å was applied. Structures were optimized with a conjugate gradient algorithm until the forces on all relaxed atoms were less than 0.02 eV/Å, and the  $1 \times 1 \times 1$  k-point grid was adopted based on the Monkhorst-Pack method [40]. The adsorption energies of Ag/Cu on the  $\gamma\text{-Al}_2\text{O}_3$  surface were calculated as follows:  $E_{ad} = E_{adsorbate + surface} - (E_{surface} + E_{atom})$ , where  $E_{adsorbate+surface}$ ,  $E_{atom}$ , and  $E_{surface}$  are the total energies of the system that adsorbed Ag/Cu, single active metal atom, and the  $\text{Al}_2\text{O}_3$  slab, respectively.  $E_{ad}$  denotes the stability of the adsorbates on the  $\gamma\text{-Al}_2\text{O}_3$  surface. Negative  $E_{ad}$  values indicate that the adsorbed state is energetically favorable.

#### 2.4. Catalytic activity test

A fixed-bed quartz tube reactor (i.d. 4 mm) was used to test the  $\text{NH}_3$ -SCO activity of the catalysts (30 mg for each testing), with the total gas flow controlled at 100 mL·min<sup>-1</sup> and the gas hourly space velocity (GHSV) as 120,000 h<sup>-1</sup>. The gas composition at the reactor inlet was  $\text{NH}_3$  (500 ppm),  $\text{O}_2$  (10 vol%), and balance  $\text{N}_2$ . The concentrations of effluent  $\text{NH}_3$  and  $\text{NO}_x$  were continuously monitored using an online FTIR spectrometer equipped with a 2-m gas cell and a DTGS detector. The turnover frequency (TOF) is defined as the number of  $\text{NH}_3$

molecules converted per surface Ag atom per second. Only  $\text{NO}$ ,  $\text{NO}_2$ ,  $\text{N}_2\text{O}$ , and  $\text{NH}_3$  were detected during the reaction. Therefore, the  $\text{NH}_3$  conversion ( $X_{\text{NH}_3}$ ),  $\text{N}_2$  selectivity ( $S_{\text{N}_2}$ ), and  $\text{N}_2\text{O}$  selectivity ( $S_{\text{N}_2\text{O}}$ ) were calculated according to Eqs. (1) and (3):

$$X_{\text{NH}_3} = (1 - \frac{[\text{NH}_3]_{\text{out}}}{[\text{NH}_3]_{\text{in}}}) \times 100\% \quad (1)$$

$$S_{\text{N}_2} = (1 - \frac{2[\text{N}_2\text{O}]_{\text{out}} + [\text{NO}]_{\text{out}} + [\text{NO}_2]_{\text{out}}}{[\text{NH}_3]_{\text{in}} - [\text{NH}_3]_{\text{out}}}) \times 100\% \quad (2)$$

$$S_{\text{N}_2\text{O}} = \frac{2[\text{N}_2\text{O}]_{\text{out}}}{[\text{NH}_3]_{\text{in}} - [\text{NH}_3]_{\text{out}}} \times 100\% \quad (3)$$

The TOF measurements were performed in separate experiments, where the  $\text{NH}_3$  conversion was maintained below 30% by varying the GHSV, and the TOFs were calculated according to Eq. (4):

$$\text{TOF} = \frac{\eta_{\text{NH}_3} \times Q \times (60V_m)}{(m \times w_{\text{Ag}} \times D_{\text{Ag}})/M_{\text{Ag}}}, \quad (4)$$

where  $\eta_{\text{NH}_3}$  is the  $\text{NH}_3$  conversion rate (< 30%),  $Q$  is the gas flow rate (L/min),  $V_m$  is equal to 22.4 L/mol,  $m$  is the mass of catalyst (g),  $w_{\text{Ag}}$  is the Ag loading (wt%),  $D_{\text{Ag}}$  is the dispersion of Ag on  $\gamma\text{-Al}_2\text{O}_3$  (%) (calculated based on the average Ag particle size from STEM images), and  $M_{\text{Ag}}$  is the relative molecular weight of Ag (g/mol; the relationship between Ag size (d) and dispersion (D) is  $d (\text{nm}) = 1.31/D$ ) [41].

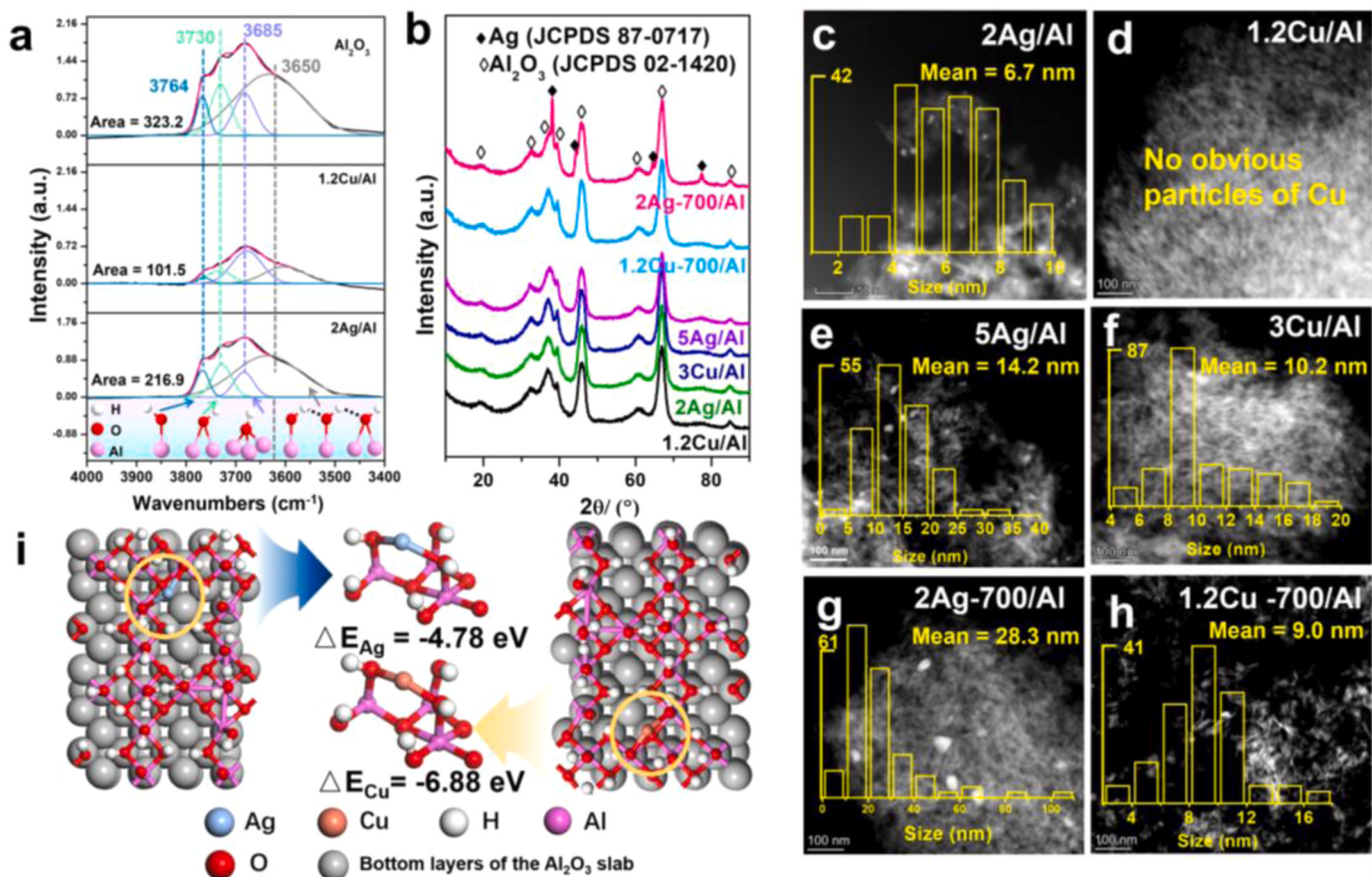


**Fig. 1.** The hydroxyl content of  $\gamma\text{-Al}_2\text{O}_3$  support loaded with Cu or Ag; a comparison of dispersion degree of Ag and Cu species on  $\gamma\text{-Al}_2\text{O}_3$ ; and DFT calculation of anchoring capability of Cu and Ag on  $\gamma\text{-Al}_2\text{O}_3$ : (a) The hydroxyl content of  $\gamma\text{-Al}_2\text{O}_3$ , 2Ag/Al and 1.2Cu/Al samples based on FTIR measurement in vacuum.; (b) XRD patterns; HAADF-STEM images of (c) 2Ag/Al, (d) 1.2Cu/Al, (e) 5Ag/Al, (f) 3Cu/Al, (g) 2Ag-700/Al, (h) 1.2Cu-700/Al; and (i) DFT calculation results of anchoring capability of Ag or Cu onto  $\gamma\text{-Al}_2\text{O}_3$  (100) surface.

### 3. Results and discussion

#### 3.1. Anchoring strength of Ag and Cu on $\text{Al}_2\text{O}_3$

Our previous studies demonstrated that Ag atoms anchor to the  $\gamma\text{-Al}_2\text{O}_3$  surface by coordinating with terminal and doubly bridging hydroxyl groups [34]. The hydroxyl content on the  $\gamma\text{-Al}_2\text{O}_3$  surface was measured by *in situ* FTIR in a high-vacuum chamber under pressure of  $< 5 \times 10^{-8}$  mbar. All tested samples underwent pretreatment at 230 °C for 1 h to remove  $\text{H}_2\text{O}$ . Based on the results shown in Fig. 1a, the peaks at 3764, 3730, and 3685  $\text{cm}^{-1}$  on  $\text{Al}_2\text{O}_3$ , 2Ag/Al, and 1.2Cu/Al samples, respectively, could be attributed to terminal hydroxyls, doubly bridging hydroxyls, and triply bridging hydroxyls. A large and broad peak detected at 3650  $\text{cm}^{-1}$  could be due to the presence of associated hydroxyl groups [42]. Compared with terminal and doubly bridging hydroxyls, triply bridging and associated hydroxyl groups usually exhibit lower net charges [42]. This phenomenon indicates that only the terminal and bridging hydroxyl groups are available as active anchoring sites for supported metals [43]. As expected, the terminal hydroxyls ( $3764 \text{ cm}^{-1}$ ) and doubly bridging hydroxyls ( $3730 \text{ cm}^{-1}$ ) on  $\gamma\text{-Al}_2\text{O}_3$  were heavily consumed after loading both Ag and Cu [44–53]. To verify if the surface hydroxyl groups on  $\text{Al}_2\text{O}_3$  could be reduced after calcination at 550 °C, a new set of experiments was designed, in which  $\text{Al}_2\text{O}_3$  was added into deionized water to form a suspension and then stirred for 2 h, followed by vacuum rotary evaporation, drying and calcination at 550 °C. These treatments barely affected the hydroxyl concentration on  $\text{Al}_2\text{O}_3$  support (Supplementary Fig. S1a). However, the hydroxyl groups on the surface of the 0.6Cu/Al, 1.8Cu/Al, 3Cu/Al, and 5Cu/Al samples clearly decreased with Cu loading (Supplementary Fig. S1b). Therefore, it can be preliminarily deduced that Cu could also be anchored through the terminal hydroxyl groups and bridging hydroxyl groups on the surface of  $\gamma\text{-Al}_2\text{O}_3$  similar to Ag. When the same atomic numbers of Ag and Cu were loaded on  $\text{Al}_2\text{O}_3$ , the detected hydroxyl peaks on the surface of  $\text{Al}_2\text{O}_3$  were integrated as 216.9 a.u. (2Ag/Al) and 101.5 a.u. (1.2Cu/Al), respectively. Hence, the utilization efficiency of hydroxyl groups by Cu atoms should be considerably higher than that by Ag atoms.

To compare the anchoring strength of Ag and Cu on  $\text{Al}_2\text{O}_3$ , the degree of agglomeration of the Ag and Cu species under the same loading or  $\text{H}_2$  pretreatment condition was investigated. As shown in Fig. 1b, the 2Ag/Al, 5Ag/Al, 1.2Cu/Al, and 3Cu/Al samples did not show obvious XRD diffraction peaks of the Ag or Cu species. This suggests that the Ag and Cu species could be highly dispersed on the  $\gamma\text{-Al}_2\text{O}_3$  surface without forming large nanoparticles under low-metal-loading conditions (Supplementary Fig. S2). The average particle sizes of the 2Ag/Al, 5Ag/Al, and 3Cu/Al samples were 6.7, 14.2, and 10.2 nm, respectively. Moreover, no obvious nanoparticles could be observed on the 1.2Cu/Al sample, as the STEM images shown in Fig. 1c–f. Even when the Cu loading increased to 1.8 wt%, Cu atoms remained as isolated atoms and/or clusters on the  $\text{Al}_2\text{O}_3$  surface without forming significant nanoparticles (Supplementary Fig. S2). This result indicates that Cu species had higher dispersion degree on  $\text{Al}_2\text{O}_3$  than Ag species. In addition, a clear difference in the agglomeration degree was observed in the 2Ag/Al and 1.2Cu/Al samples after  $\text{H}_2$  pretreatment. The 2Ag-700/Al sample showed strong XRD diffraction peaks ascribed to the Ag crystal phase (Fig. 1b), and the average particle size of Ag was 28.3 nm (Fig. 1g). However, as shown in Fig. 1b, no significant Cu diffraction peaks were observed on the 1.2Cu-700/Al sample, and the STEM image also showed that the average particle size of Cu was only 9.0 nm (Fig. 1h), much smaller than that of Ag particles (Fig. 1g). Because  $\text{H}_2$  reduction could break the Metal–O bond to induce the formation of metal nanoparticles, the higher Ag agglomeration degree could indirectly reflect that the anchoring strength of Ag on  $\text{Al}_2\text{O}_3$  was much weaker than that of Cu in this study [29,32].

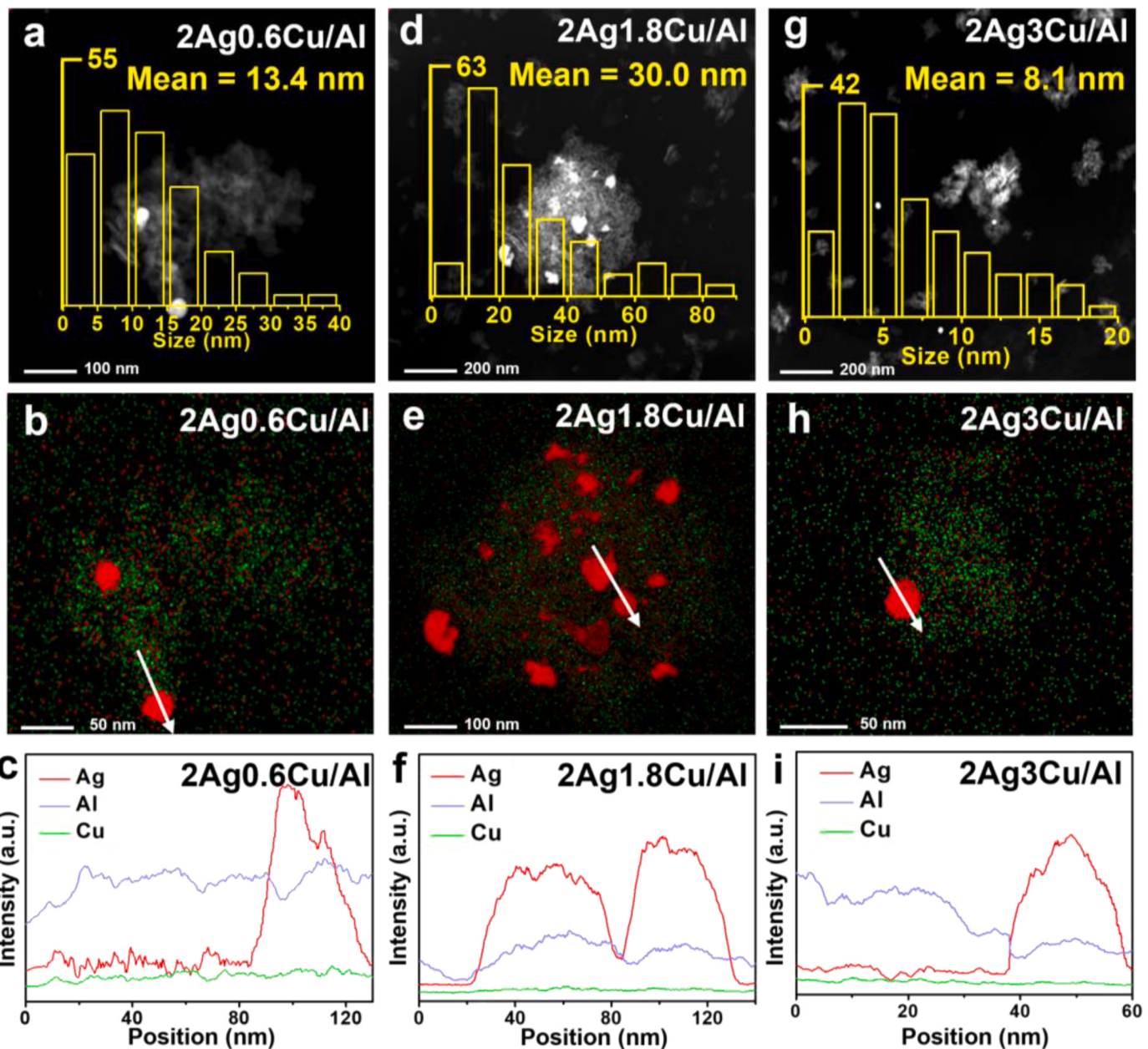
DFT calculations were performed to confirm this hypothesis and investigate the interaction between Ag and Cu species and hydroxyl

groups. Our previous study demonstrated that the terminal hydroxyl groups on the (100) surface of  $\text{Al}_2\text{O}_3$  were the anchoring sites of Ag [34]. Accordingly, we calculated the interaction between Ag and Cu atoms and terminal hydroxyls on the (100) surface of  $\gamma\text{-Al}_2\text{O}_3$ . The relaxed structures of Ag or Cu binding on the hydroxylated (100) surfaces of  $\gamma\text{-Al}_2\text{O}_3$  are presented in Fig. 1i. The Ag and Cu atoms can be stably bonded to the terminal hydroxyl sites, demonstrating that the (100) surface of  $\gamma\text{-Al}_2\text{O}_3$  could anchor these atoms. Stable bridge-like structures with double terminal hydroxyl groups were formed on the (100) surface of  $\gamma\text{-Al}_2\text{O}_3$  (Fig. 1i; orange circles), and the adsorption energies of Ag and Cu in the models were calculated as  $-4.78$  and  $-6.88$  eV, respectively. This result shows that Cu atoms could be more stably anchored to the (100) surfaces of  $\gamma\text{-Al}_2\text{O}_3$  than Ag atoms.

The experimental results and DFT calculations demonstrated that Cu atoms could exhibit higher hydroxyl utilization efficiency and stronger anchoring strength onto the  $\gamma\text{-Al}_2\text{O}_3$  surface compared to Ag atoms. These results suggest the high probability that Cu atoms preferentially preoccupy the terminal hydroxyl groups and cause the Ag atoms to agglomerate when the hydroxyl groups are insufficient on the  $\gamma\text{-Al}_2\text{O}_3$  surface.

#### 3.2. Effect of Cu loading on Ag particle size

The microstructure and compositional distribution of the nanocrystals were further investigated by STEM and EDS mapping to explore the effect of Cu loading on the Ag particle size in  $\text{Ag-CuO}_x/\text{Al}_2\text{O}_3$  catalysts. As shown in Fig. 2a–c, the Cu introduction considerably increased the size of the metal particles compared with the catalyst with only Ag. The EDS mapping results further confirmed that the composition of the observed metal particles was dominated by Ag (Fig. 2b, e, h). In contrast, Cu was mainly highly dispersed on the support surface. The sizes of Ag particles in 2Ag0.6Cu/Al, 2Ag1.8Cu/Al, and 2Ag3Cu/Al were 13.4, 30.0, and 8.1 nm, respectively, which were larger than that in the 2Ag/Al<sub>2</sub>O<sub>3</sub> sample (6.7 nm; Fig. 1c). These results indicate that the Cu introduction obviously promoted Ag agglomeration. Notably, there was an optimal Cu loading to promote Ag agglomeration on the  $\text{Al}_2\text{O}_3$  surface. The Ag particle size first increased and then decreased with increasing Cu loading, and the maximum value was reached when the Ag:Cu molar ratio was 2:3 (i.e., 2Ag1.8Cu/Al). This was due to the insufficient occupation of hydroxyl groups at low Cu loadings and the Ag redispersion on CuO particles at high Cu loadings. When the Cu loading was low, the anchoring sites were not fully occupied, and Ag could still be anchored and dispersed to a certain extent. Further, the Ag<sub>NPs</sub> observed in the 2Ag0.6/Al, 2Ag1.8Cu/Al, and 2Ag3Cu/Al samples all exhibited the characteristic lattice parameters of Ag (111) (Supplementary Fig. S3). The EDS line scanning results (Fig. 2c, f, i) reveal that the Cu element intensity was similar to or lower than that of the Al element. Moreover, the content of Cu species did not change considerably during the entire scanning interval. The Cu species did not show a higher signal, even in the region with a high Ag concentration. Therefore, the highly dispersed Cu species could not form an ordered CuO<sub>x</sub> interface to anchor Ag. When the Cu loading was low, the anchoring sites were not fully occupied, and Ag could still be anchored and dispersed to a certain extent on  $\text{Al}_2\text{O}_3$ . However, when the Cu loading reached the optimal level and continued to increase, the Cu species formed large CuO particles (Supplementary Fig. S4) and forced Ag to diffuse from  $\text{Al}_2\text{O}_3$  to the CuO surface and redisperse (Supplementary Fig. S5). The DFT calculation results (Supplementary Fig. S6 for the adsorption energy of Ag on the CuO surface, which was  $E_{\text{Ag}} = -1.87$  eV) showed that the CuO surface was indeed favorable for dispersing Ag. Therefore, the CuO particles generated under high Cu loading could act as additional anchoring sites for Ag to promote the redispersion of Ag species.



16

**Fig. 2.** HAADF-STEM, EDS mapping, and line scanning images of  $2\text{Ag}_x\text{Cu}/\text{Al}$  samples: **a, b, c**  $2\text{Ag}0.6\text{Cu}/\text{Al}$ ; **d, e, f**  $2\text{Ag}1.8\text{Cu}/\text{Al}$ ; and **g, h, i**  $2\text{Ag}3\text{Cu}/\text{Al}$ . Red: Ag; Green: Cu.

### 3.3. Effect of Cu loading on the charge state of Ag

The UV-vis spectra of the catalysts with 2 wt% Ag and different Cu loadings on  $\text{Al}_2\text{O}_3$  are presented in Fig. 3a. The peak at 235 nm was attributed to  $\text{Ag}^+$  ions [54]. The peak at 280 nm was assigned to the UV absorption of  $\text{Ag}^{6+}$  clusters, and the peaks at 338 and 430 nm were assigned to the surface plasmon absorption of  $\text{Ag}^0$  clusters and  $\text{Ag}_{\text{NPs}}$ , respectively [55,56]. Cu species were mainly observed at 245, 299, 352, and 624 nm [26,57,58]. Therefore, among all the samples measured, only  $2\text{Ag}1.8\text{Cu}/\text{Al}$  showed a characteristic peak of  $\text{Ag}^0$  at 338 nm, indicating that  $\text{Ag}_{\text{NPs}}$  possibly existed in the  $2\text{Ag}1.8\text{Cu}/\text{Al}$  catalyst. This phenomenon can also be confirmed by the XRD results (Fig. 3b). Typical diffraction peaks of  $\gamma\text{-Al}_2\text{O}_3$  were present for all samples, while no Ag-containing phases were observed except for the  $2\text{Ag}1.8\text{Cu}/\text{Al}$

catalyst. In case of the  $2\text{Ag}1.8\text{Cu}/\text{Al}$  catalyst, obvious diffraction peaks at 20 of  $38.1^\circ$ ,  $44.3^\circ$ ,  $64.5^\circ$ , and  $77.4^\circ$  were observed, corresponding to the (111), (200), (220), and (311) lattice planes of Ag. This indicates that the Ag species within this catalyst were in a high aggregation state when the Ag:Cu ratio was 2:3. However, when the Cu loading was lower or higher than this ratio, no significant diffraction peaks of  $\text{Ag}^0$  species were observed. This is because the low Cu loading was insufficient to make Ag fully agglomerate, and the excessively high Cu loading could lead to the formation of  $\text{CuO}$  (Supplementary Fig. S7) to redisperse Ag.

Further, XAFS measurements were conducted to study the valence state and coordination condition of Ag species on  $2\text{Ag}_x\text{Cu}/\text{Al}$  samples with different Ag:Cu ratios ( $2\text{Ag}0.6\text{Cu}/\text{Al}$ ,  $2\text{Ag}1.8\text{Cu}/\text{Al}$ , and  $2\text{Ag}3\text{Cu}/\text{Al}$ ), using Ag foil,  $\text{Ag}_2\text{O}$ , and  $\text{AgNO}_3$  as references. The normalized Ag-K XANES (Fig. 3c) shows that the white line intensities of all  $2\text{Ag}_x\text{Cu}/\text{Al}$

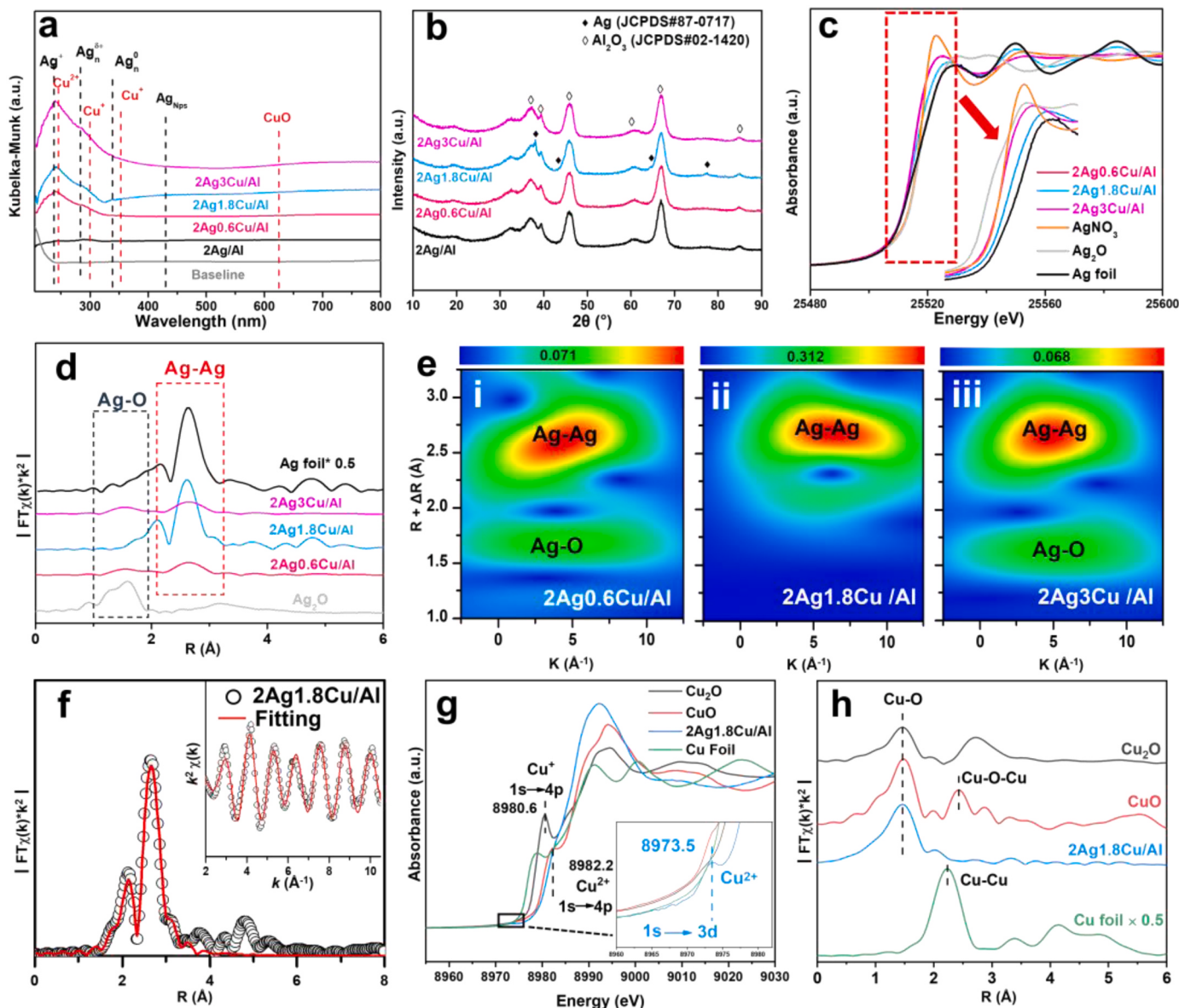


**Fig. 3.** Structure characterization of the 2AgxCu/Al samples: (a) UV–vis absorption spectra; (b) XRD patterns; (c) Ag K-edge XANES; (d) Ag K-edge EXAFS; and (e) WT of (i) 2Ag0.6Cu/Al, (ii) 2Ag1.8Cu/Al, and (iii) 2Ag3Cu/Al samples; (f) the 2Ag1.8Cu/Al EXAFS fitting curve in R- and k-(inset) spaces; (g) Cu K-edge XANES; (h) Cu K-edge EXAFS.

catalysts were between those of Ag foil and AgNO<sub>3</sub>, indicating that the Ag species in the 2AgxCu/Al catalysts were in a mixed form of Ag<sup>0</sup> and Ag<sup>+</sup>. The valence states of Ag species in 2Ag0.6Cu/Al and 2Ag3Cu/Al were similar because their white lines almost overlapped. However, the Ag species in the 2Ag1.8Cu/Al sample were much closer to Ag foil than those in 2Ag0.6Cu/Al and 2Ag3Cu/Al [59,60]. This indicates that more metallic Ag species existed in the 2Ag1.8Cu/Al sample, consistent with the X-ray photoelectron spectroscopy results (Supplementary Fig. S8). This conclusion was further confirmed by Fourier-transformed Ag-K EXAFS, as shown in Fig. 3d. The characteristic peak of the Ag–Ag metallic bond at 2.67 Å (phase uncorrected) was observed for the Ag foil as well as the 2Ag0.6Cu/Al, 2Ag1.8Cu/Al, and 2Ag3Cu/Al samples [61]. In addition, the Ag–Ag coordination shell intensity for 2Ag1.8Cu/Al was much stronger than that for the 2Ag0.6Cu/Al and 2Ag3Cu/Al samples.

The wavelet transform (WT) analysis of the  $k^2$ -weighted EXAFS signal was performed to distinguish the backscattering atoms in greater detail, and the WT contour plots are shown in Fig. 3e. Two WT intensity maxima were observed for the 2Ag0.6Cu/Al and 2Ag3Cu/Al samples,

with one at 1.5–2.0 Å due to the Ag–O coordination shell and the other at ca. 2.2–3.0 Å, which could be assigned to the Ag–Ag coordination shell (Fig. 3e–i,iii). In contrast, the 2Ag1.8Cu/Al sample only displayed one WT maximum at ca. 2.2–3.0 Å owing to the Ag–Ag coordination shell (Fig. 3h,ii).

The EXAFS curve fitting was conducted to acquire quantitative structural parameters of Ag in the 2Ag1.8Cu/Al catalyst, and the fitting parameters and curves are shown in Fig. 3f. The coordination numbers of Ag–Ag bonds were ca. 2.0, 7.1, and 2.0 in 2Ag0.6Cu/Al, 2Ag1.8Cu/Al, and 2Ag3Cu/Al, respectively [62–64] (Supplementary Table S1 and Fig. S9). In addition, judging from the colormap intensity, the Ag–Ag bond intensity in the 2Ag1.8Cu/Al sample was considerably higher than those in 2Ag0.6Cu/Al and 2Ag3Cu/Al. These results indicate that there were more Ag nanoparticles within the 2Ag1.8Cu/Al catalyst, and the lower or higher Cu loading could make Ag species more dispersed [32, 65]. Fig. 3g presents the XANES patterns of the Cu K-edge for the 2Ag1.8Cu/Al catalyst and reference samples. The peak observed at 8982.2 eV indicated electron transfer between the 1 s and 3d orbitals of

the Cu<sup>2+</sup> species, confirming the presence of Cu<sup>2+</sup> species in the 2Ag1.8Cu/Al catalyst. In addition, the 8980.6 and 8982.2 eV peaks correspond to electron transfers from the 1 s to 4p orbitals of Cu<sup>+</sup> in Cu<sub>2</sub>O and Cu<sup>2+</sup> in CuO, respectively [66]. In the R-space EXAFS (Fig. 3h), a discernible peak was observed in the Cu-containing samples, attributed to the Cu–O coordination shell (*ca.* 1.4 Å, phase uncorrected). In addition, no evidence of Cu–Cu, Cu–Ag, or Cu–O–Cu scattering was detected in 2Ag0.6Cu/Al, 2Ag1.8Cu/Al, and 2Ag3Cu/Al, respectively, providing further evidence that Cu predominantly existed as a highly dispersed Cu<sup>2+</sup> and Cu<sup>+</sup> species.

Because the Cu introduction affects Ag dispersion, we further examined the influence of the Cu and Ag loading sequence on the Ag dispersion state. Catalysts represented as 1.8Cu/2Ag/Al and 2Ag/1.8Cu/Al were prepared by sequentially supporting Ag or Cu and then Cu or Ag, respectively. Although both catalysts did not show significant Ag characteristic peaks in the XRD patterns (Supplementary Fig. S10), significant peaks were observed in the STEM results for the 1.8Cu/2Ag/Al and 2Ag/1.8Cu/Al samples. The attached Ag particles have average particle sizes of 15.3 and 24.7 nm, respectively (Supplementary Fig. S10), while Cu remains highly dispersed on the Al<sub>2</sub>O<sub>3</sub> surface. These results clearly show that Cu atoms could preferentially occupy the terminal hydroxyl groups regardless of the loading order. Thus, there were not enough anchoring sites on the γ-Al<sub>2</sub>O<sub>3</sub> surface, leading to the aggregation of Ag atoms.

### 3.4. Oxygen activation capacity and NH<sub>3</sub>-SCO performance

Our previous studies have proven that the excellent O<sub>2</sub> activation ability of Ag<sub>NPs</sub> with large particle sizes was the main reason for the superior NH<sub>3</sub>-SCO performance [29,32]. Therefore, we further compared the oxygen activation ability and the corresponding NH<sub>3</sub>-SCO performance between the samples with different Ag:Cu ratios.

*In situ* Raman spectroscopy was used to observe the state of oxygen species on the surface of different samples. As shown in Fig. 4a, under 10 vol% O<sub>2</sub>/N<sub>2</sub>, the peaks at 245, 546, 670, 907, and 1038 cm<sup>-1</sup> were attributed to adsorbed atomic oxygen (O), peroxy (O<sub>2</sub><sup>·</sup>), molecular O<sub>2</sub>, O<sub>2</sub> with migrated electronic states, and superoxide (O<sub>2</sub><sup>·-</sup>), respectively [67–69]. To confirm that the Raman shifts for different oxygen species are located at the same positions as reported in literature, we pretreated the samples with N<sub>2</sub> or 10 vol% H<sub>2</sub>/N<sub>2</sub> to exclude the influence of moisture and other impurities (Supplementary Fig. S11). The O<sub>2</sub> activation capacity of single-metal catalysts was tested using *in situ* Raman spectroscopy, and these catalysts were found to have poor O<sub>2</sub> activation ability (Supplementary Fig. S12). Compared to the single-metal catalysts, the 2AgxCu/Al serial catalysts exhibited excellent O<sub>2</sub> activation ability due to the addition of Cu, which induced the aggregation of Ag species. On the 2Ag0.6Cu/Al sample, as shown in Fig. 4a, the surface oxygen species were dominated by molecular oxygen, with a strong Raman shift observed at 670 cm<sup>-1</sup>. The activated oxygen species, including O<sub>2</sub> with migrated electronic states at 907 cm<sup>-1</sup> and O<sub>2</sub><sup>·-</sup> at

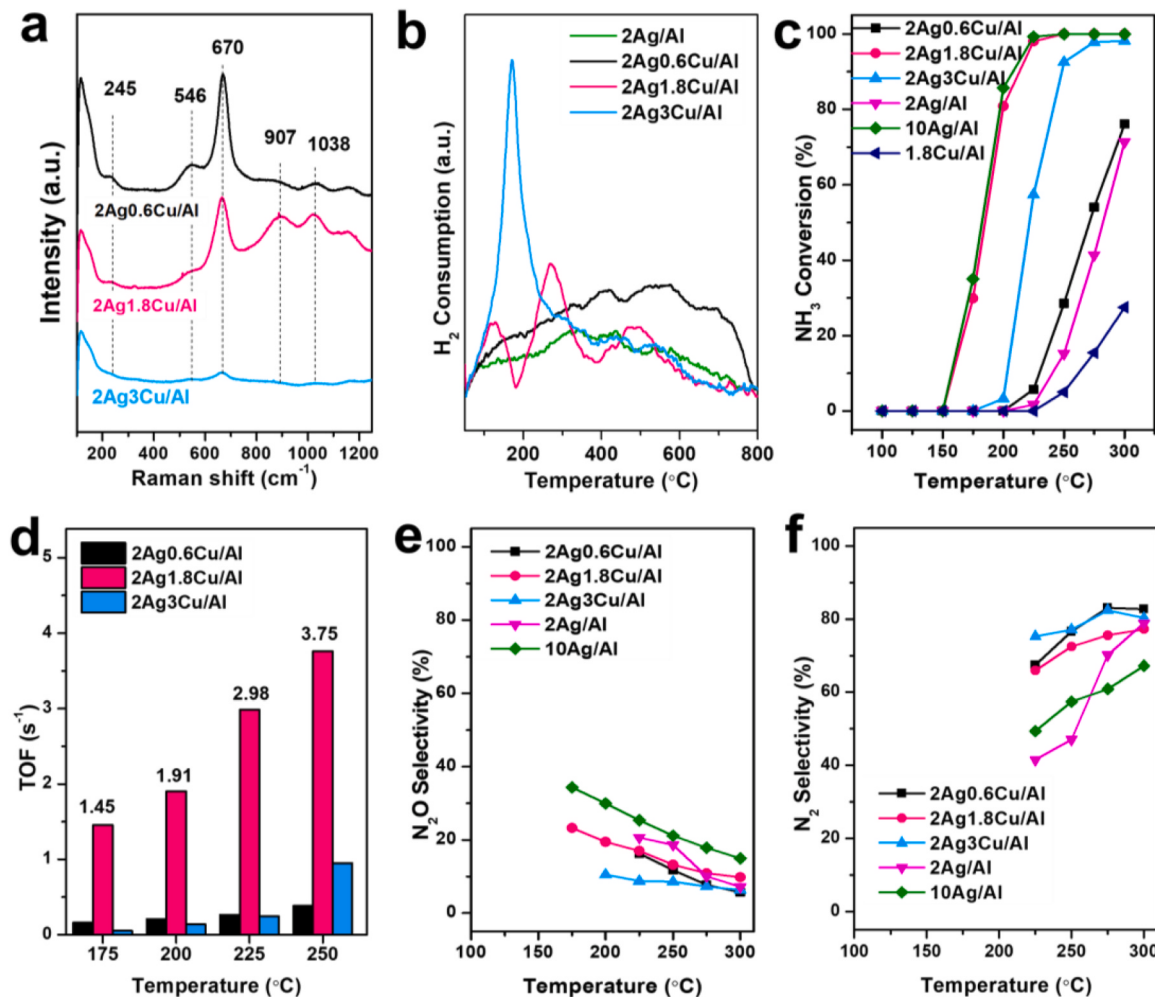


**Fig. 4.** *In situ* Raman spectra, H<sub>2</sub>-TPR profiles, NH<sub>3</sub>-SCO performance on 2Ag0.6Cu/Al, 2Ag1.8Cu/Al, and 2Ag3Cu/Al catalysts: (a) *In situ* Raman spectra under 10 vol% O<sub>2</sub>/N<sub>2</sub> at 175 °C, (b) H<sub>2</sub>-TPR profiles, (c) NH<sub>3</sub>-SCO activity results, (d) calculated TOF of NH<sub>3</sub> conversion, (e) N<sub>2</sub>O selectivity, and (f) N<sub>2</sub> selectivity. Reaction conditions: NH<sub>3</sub> = 500 ppm, O<sub>2</sub> = 10 vol%, and GHSV = 120,000 h<sup>-1</sup>.

$1038\text{ cm}^{-1}$ , were also present on 2Ag0.6Cu/Al. Obviously, the surface oxygen species on the 2Ag1.8Cu/Al sample were more abundant, and the proportion of activated oxygen species was significantly increased compared with that on 2Ag0.6Cu/Al. Moreover, the abundance of activated oxygen species on 2Ag1.8Cu/Al was greater than that of the other two oxygen species ( $\text{O}_2$  with migrated electronic states and superoxide) at different temperatures (Supplementary Figs. S13 and S14). In contrast, except for the weak molecular oxygen species ( $670\text{ cm}^{-1}$ ), almost no other surface oxygen species were observed on the 2Ag3Cu/Al sample. These results suggest that the 2Ag1.8Cu/Al catalyst exhibited a much higher oxygen activation capacity due to the presence of a larger proportion of metallic Ag<sub>NPs</sub>, which is consistent with our previous findings [31,32].

Similar conclusions can be drawn from H<sub>2</sub>-TPR results. As shown in Fig. 4b, the 2Ag/Al and 2Ag0.6Cu/Al samples did not show obvious H<sub>2</sub> consumption peaks at temperatures below 300 °C. The low-temperature H<sub>2</sub> consumption peak gradually became more pronounced in samples with higher Cu contents. Notably, the reduction temperature of the 2Ag1.8Cu/Al sample (123 °C) was considerably lower than that of 2Ag3Cu/Al (175 °C), indicating that 2Ag1.8Cu/Al had a higher redox performance in the low-temperature range.

Further, we tested the 2Ag0.6Cu/Al, 2Ag1.8Cu/Al, and 2Ag3Cu/Al samples for NH<sub>3</sub>-SCO reaction using 2Ag/Al, 10Ag/Al, and 1.8Cu/Al samples as references to investigate the effect of Cu addition on the catalytic activity. Fig. 4c-f show that the low-loading single-component Ag or Cu samples (2Ag/Al or 1.8Cu/Al) showed poor NH<sub>3</sub>-SCO activity, with NH<sub>3</sub> conversion below 20% at 250 °C. The activity of the 2AgxCu/Al serial catalysts was considerably higher than that of the single-component catalyst, particularly when the Ag:Cu molar ratio was 2:3 (2Ag1.8Cu/Al). The activity of the 2Ag1.8Cu/Al sample was considerably improved with NH<sub>3</sub> conversion above 90% at 200 °C, which was almost identical to that of 10Ag/Al. To maintain consistent activity, the 'pre-occupied-anchoring-site' strategy could considerably reduce the catalyst cost to ca. one-fifth of that of the pure Ag-based catalyst. The calculated TOF results further indicate that the TOF of NH<sub>3</sub> on the 2Ag1.8Cu/Al sample was ca. 10 and 5 times those on the 2Ag0.6Cu/Al and 2Ag3Cu/Al samples, respectively (at 250 °C; Fig. 4d). These results correlate well with the changing trend of metallic Ag<sub>NPs</sub> content within the samples. Thus, Cu introduction led to the agglomeration of low-loading Ag (2 wt%) to form Ag<sub>NPs</sub>, improving its oxygen activation ability and, thus, the NH<sub>3</sub>-SCO performance. In addition, compared to pure Ag-based catalysts, Cu introduction significantly reduced N<sub>2</sub>O, NO, and NO<sub>2</sub> formation (Fig. 4e and Supplementary Fig. S15), thus improving the N<sub>2</sub> selectivity (Fig. 4f). This is also consistent with the results reported in the literature [26,70]. Introducing Cu will cause changes in the existence state of Ag species and thus affect the oxygen activation ability, which may be the main reason for affecting N<sub>2</sub> selectivity. The oxygen species on the 2Ag0.6Cu/Al surface were mainly adsorbed O<sub>2</sub> molecules (Fig. 4a), which can only overoxidize NH<sub>3</sub> into small amounts of NO and N<sub>2</sub>O (Fig. S15). Therefore, it showed a relatively low NH<sub>3</sub> conversion and slightly better N<sub>2</sub> selectivity. However, a large amount of highly active O<sub>2</sub><sup>-</sup> and electronically transferred O appeared on the 2Ag1.8Cu/Al surface, causing NH<sub>3</sub> to be overoxidized into N<sub>2</sub>O, NO, and NO<sub>2</sub>. The presence of numerous N<sub>2</sub>O molecule was the main reason for its low N<sub>2</sub> selectivity (Fig. S15). As the Cu loading increased, the Ag<sub>NPs</sub> on the 2Ag3Cu/Al surface were redispersed again, which reduced the O<sub>2</sub> activation ability of Ag<sub>NPs</sub> and amplified the catalytic effect of Cu species. However, because of the weak O<sub>2</sub> activation ability of Cu species, N<sub>2</sub>O production was considerably reduced, increasing N<sub>2</sub> selectivity on 2Ag3Cu/Al (Fig. S15).

To further study the impact of introducing Cu species on catalyst stability, the 2Ag-700/Al samples were prepared for comparison with 2Ag1.8Cu/Al because the sizes of Ag<sub>NPs</sub> in both samples were similar. Indeed, the NH<sub>3</sub> conversion on 2Ag-700/Al and 2Ag1.8Cu/Al was nearly identical at 100 °C–300 °C (Supplementary Fig. S16a). However, the 2Ag1.8Cu/Al catalyst maintained 100% NH<sub>3</sub> conversion at 400 °C for

more than 48 h, while 2Ag-700/Al achieved only 100% NH<sub>3</sub> conversion for 2 h and completely lost the NH<sub>3</sub>-SCO activity after 8 h (Supplementary Fig. S16b). This may be because the hydroxyl anchoring sites on the surface of the 2Ag-700/Al catalyst prepared by the H<sub>2</sub> reduction method still existed [29,71], and the Ag<sub>NPs</sub> were redispersed during the NH<sub>3</sub>-SCO reaction, resulting in a rapid decrease in activity. However, most of the hydroxyl binding sites on 2Ag1.8Cu/Al were occupied by Cu, and there was a lack of abundant hydroxyl binding sites available to redisperse Ag during the NH<sub>3</sub>-SCO process. Hence, the 2Ag1.8Cu/Al sample consistently maintained excellent stability during the NH<sub>3</sub>-SCO reaction.

To assess the resistance of the catalysts to H<sub>2</sub>O, CO<sub>2</sub>, and SO<sub>2</sub>, NH<sub>3</sub>-SCO reactions were conducted under dry/wet, CO<sub>2</sub> and SO<sub>2</sub> on/off conditions at 400 °C (Supplementary Fig. S17). H<sub>2</sub>O exerted a noticeable effect on NH<sub>3</sub>-SCO of 2Ag0.6Cu/Al, with NH<sub>3</sub> conversion rapidly decreasing from 100% to ca. 91% at 400 °C within 10 min after H<sub>2</sub>O addition. However, for 2Ag0.6Cu/Al, the NH<sub>3</sub> conversion gradually recovered to the initial level within 10 min of turning off the H<sub>2</sub>O. In contrast, the 2Ag1.8Cu/Al and 2Ag3Cu/Al catalysts were less pronouncedly affected by H<sub>2</sub>O incorporation into the reaction atmosphere. In previous studies, H<sub>2</sub>O competed with NH<sub>3</sub> for adsorption, where larger Ag<sub>NPs</sub> tended to adsorb NH<sub>3</sub> more readily and smaller Ag<sub>NPs</sub> had a higher affinity for H<sub>2</sub>O molecules [71]. Given that the surface of 2Ag0.6Cu/Al contained smaller Ag<sub>NPs</sub>, the competitive adsorption effect of H<sub>2</sub>O was more pronounced. However, the larger size of Ag<sub>NPs</sub> on the 2Ag1.8Cu/Al surface reduced the impact of competitive H<sub>2</sub>O adsorption. Although the size of Ag<sub>NPs</sub> in the 2Ag3Cu/Al sample was smaller than that in 2Ag1.8Cu/Al, Cu also served as an active center for NH<sub>3</sub> adsorption and oxidation. Consequently, with increasing NH<sub>3</sub> adsorption sites, the competitive adsorption effect caused by H<sub>2</sub>O was diminished. Therefore, the H<sub>2</sub>O tolerance of 2Ag1.8Cu/Al and 2Ag3Cu/Al was better than that of 2Ag0.6Cu/Al.

It was also observed that 1000 ppm CO<sub>2</sub> had a remarkable impact on the NH<sub>3</sub>-SCO activity of the 10Ag/Al catalyst. The NH<sub>3</sub> conversion on 10Ag/Al rapidly decreased from 100% to less than 20% within 20 min of CO<sub>2</sub> introduction. Adding Cu to the catalyst component enhanced the CO<sub>2</sub> resistance to a certain extent. With higher Cu loading, the negative impact of CO<sub>2</sub> was less pronounced. For example, the 2Ag1.8Cu/Al and 2Ag3Cu/Al catalysts were almost unaffected by CO<sub>2</sub>, maintaining 100% NH<sub>3</sub> conversion at 400 °C. This may be attributed to Cu acting as a sacrificial site and introducing Cu that alleviated the competitive CO<sub>2</sub> and NH<sub>3</sub> adsorption on Ag<sub>NPs</sub> [72,73]. Furthermore, CO<sub>2</sub> conversion experiments were performed using 2Ag-400/Al, 2Ag-700/Al, and 2Ag-900/Al catalysts (Supplementary Fig. S18) to exclude the effect of size. The results showed that with the CO<sub>2</sub> introduction, the NH<sub>3</sub> conversion rate in all samples decreased rapidly, and the activity gradually returned to a certain level after CO<sub>2</sub> was removed. Therefore, the CO<sub>2</sub> tolerance of the catalyst was independent of the size of Ag<sub>NPs</sub> [71].

Usually, Ag-based catalysts are very sensitive to SO<sub>2</sub> poisoning. However, in this study, the Ag-CuO<sub>x</sub>/Al<sub>2</sub>O<sub>3</sub> catalysts exhibited high tolerance to SO<sub>2</sub>, and their sulfur resistance increased with increasing CuO<sub>x</sub> loading. For instance, the 2Ag3Cu/Al sample was almost unaffected by SO<sub>2</sub> addition at 400 °C, while the 10Ag/Al sample became completely inactive after 20 min of SO<sub>2</sub> introduction (Supplementary Fig. S17). SO<sub>2</sub> switching experiments were conducted on 2Ag-400/Al, 2Ag-700/Al, and 2Ag-900/Al to eliminate the influence of Ag<sub>NPs</sub> size, and the results are presented in Fig. S18. These pure 2Ag-T/Al catalysts lost their NH<sub>3</sub>-SCO activity completely within 20 min of introducing SO<sub>2</sub>, and the activity did not recover after SO<sub>2</sub> was removed. SO<sub>2</sub> showed a substantial poisoning effect on pure Ag-based catalysts, independent of the Ag<sub>NPs</sub> size [74]. In the Ag-CuO<sub>x</sub>/Al<sub>2</sub>O<sub>3</sub> catalysts, the resistance to SO<sub>2</sub> increased with Cu loading. This could be attributed to the fact that Cu acted as SO<sub>2</sub> adsorption sites and sacrificial sites to a certain extent. Once the CuO<sub>x</sub> was sulfated, it was easy to form CuSO<sub>4</sub> and continue to adsorb NH<sub>3</sub>. Moreover, the adsorbed NH<sub>3</sub> was not easy to desorb and activate and would subsequently react with sulfate to form (NH<sub>4</sub>)<sub>2</sub>SO<sub>4</sub>.

[75]. Therefore, increasing the Cu loading actually induced more sacrificial sites, considerably alleviating the SO<sub>2</sub> poisoning of the active centers of AgNPs, thereby enhancing the sulfur resistance of the catalyst.

Therefore, the co-existence of Ag and CuO<sub>x</sub> species in the catalysts reported in this work improved the resistance to H<sub>2</sub>O, CO<sub>2</sub>, and SO<sub>2</sub> to a certain extent, which was very beneficial for practical applications. Furthermore, the sequential impregnation of Ag and Cu significantly reduced the AgNPs agglomeration (Supplementary Fig. S10). This reduction in agglomeration played a pivotal role in causing the lower NH<sub>3</sub>-SCO observed on 1.8Cu/2Ag/Al and 2Ag/1.8Cu/Al compared with that on 1.8Cu2Ag/Al (Supplementary Fig. S19). NH<sub>3</sub>-TPD results suggested that the differences in the acidity of acid sites among 2Ag1.8Cu/Al, 1.8Cu/2Ag/Al, and 2Cu/1.8Ag/Al were insignificant (Supplementary Fig. S20).

However, the NH<sub>3</sub>-SCO activity of the catalyst did not increase linearly with the increase in the AgNPs size under limited Ag loading. The size of AgNPs usually affects the Ag oxidation state; e.g., larger AgNPs were associated with higher Ag metal content (as shown in Fig. 3c). The increase in the metal (Ag<sup>0</sup>) content was conducive to improving the NH<sub>3</sub>-SCO activity. However, the number of active sites was considerably reduced when the nanoparticle size exceeded a certain threshold, resulting in a decrease in the apparent activity [71]. In addition, Cu species also exhibited certain NH<sub>3</sub>-SCO activity, which could be increased with elevated Cu loading [76]. Therefore, the excellent NH<sub>3</sub>-SCO performance of the 2Ag1.8Cu/Al catalyst was mainly attributed to the combined effects of increased AgNPs size, lowered Ag valence state, and Cu activity, all of which originated from the Cu 'pre-occupied-anchor-site' effect.

In addition, we conducted a mechanistic study on 10Ag/Al and 2Ag1.8Cu/Al catalysts by *in situ* DRIFTS (Supplementary Section 10; Figs. S21–S29). The NH<sub>3</sub> adsorbed on the 10Ag/Al catalyst underwent profound dehydrogenation, forming N<sub>2</sub><sup>−</sup> species. The oxidation of these N<sub>2</sub><sup>−</sup> species resulted in substantial N<sub>2</sub>O production, thereby establishing the primary influence of intermediate product N<sub>2</sub><sup>−</sup> on the N<sub>2</sub> selectivity of the 10Ag/Al catalyst. However, introducing Cu atoms could inhibit the deep dehydrogenation of −NHx species to −N species and thus limit the formation of N<sub>2</sub><sup>−</sup> [31,77,78]. Although the −NHx species on the 2Ag1.8Cu/Al catalyst would also be oxidized to produce N<sub>2</sub>O, the N<sub>2</sub>O yield was significantly lower than that of 10Ag/Al. Therefore, the introduction of Cu atoms not only inhibited N<sub>2</sub><sup>−</sup> formation on the

2Ag1.8Cu/Al catalyst but also facilitated the generation of intermediate products such as −N<sub>2</sub>H<sub>4</sub> and −HNO, resulting in a substantial N<sub>2</sub> selectivity enhancement during NH<sub>3</sub>-SCO.

### 3.5. A universal mechanism of pre-occupied-anchor-site strategy

We showed that Cu atoms could occupy the anchor sites of Ag to agglomerate Ag into Ag<sup>0</sup> nanoparticles. It was hypothesized that when other metals with greater anchoring strength to the hydroxyl group than Ag exist on Al<sub>2</sub>O<sub>3</sub>, the co-loading of Ag with these metals might also lead to Ag agglomeration into large AgNPs on the Al<sub>2</sub>O<sub>3</sub> surface. For this purpose, the anchoring strength of several transition metals to the hydroxyl groups on Al<sub>2</sub>O<sub>3</sub> was calculated, and the results are displayed in Fig. 5. The energies of Co, Mn, Fe, and Ni anchoring to the terminal hydroxyl groups on Al<sub>2</sub>O<sub>3</sub> were −8.34, −9.49, −8.69, and −4.83 eV, respectively, all more negative than the anchoring energy of Ag (−4.78 eV). These results suggest that the transition metals considered could have a high potential to preoccupy the anchor sites of Ag. Experimentally, when Al<sub>2</sub>O<sub>3</sub> was loaded with these metals, the concentrations of terminal and doubly bridging hydroxyl groups on the Al<sub>2</sub>O<sub>3</sub> surface were greatly reduced (Supplementary Fig. S30).

The NH<sub>3</sub>-SCO activity test results revealed that the catalytic performance of AgMO<sub>x</sub>/Al (M = other metals coloaded with Ag) was much higher than that of 2Ag/Al (Fig. 6a). The XRD patterns of 2Ag1.6Co/Al, 2Ag1.5Mn/Al, 2Ag1.6Fe/Al, and 2Ag1.6Ni/Al all showed characteristic peaks of Ag<sup>0</sup> (Fig. 6b). These results suggest that Co, Mn, Fe, and Ni preoccupied the anchor sites of Ag, leading to Ag agglomeration and resulting in enhanced NH<sub>3</sub>-SCO activity. The STEM results also confirmed this conclusion. For example, the average sizes of AgNPs in 2Ag1.6Co/Al, 2Ag1.5Mn/Al, 2Ag1.6Fe/Al, and 2Ag1.6Ni/Al were 26.6, 48.8, 11.9, and 25.8 nm, respectively, and only Ag was heavily agglomerated, whereas Co, Mn, Fe, and Ni were highly dispersed on the Al<sub>2</sub>O<sub>3</sub> surface. In addition, the main byproduct during the NH<sub>3</sub>-SCO reaction in the AgMO<sub>x</sub>/Al catalyst system was N<sub>2</sub>O (Supplementary Figs. S31–S34 for product analysis), a characteristic byproduct of catalysts with AgNPs as active centers. Considering that 5.4Co/Al, 5.1Mn/Al, 5.2Fe/Al, and 5.4Ni/Al showed relatively low NH<sub>3</sub>-SCO activity, the main active centers of AgMO<sub>x</sub>/Al catalysts were still AgNPs. This suggests that Co, Mn, Fe, and Ni also showed a 'pre-occupied-anchor-site' effect. Notably, the various metals used as placeholders showed different

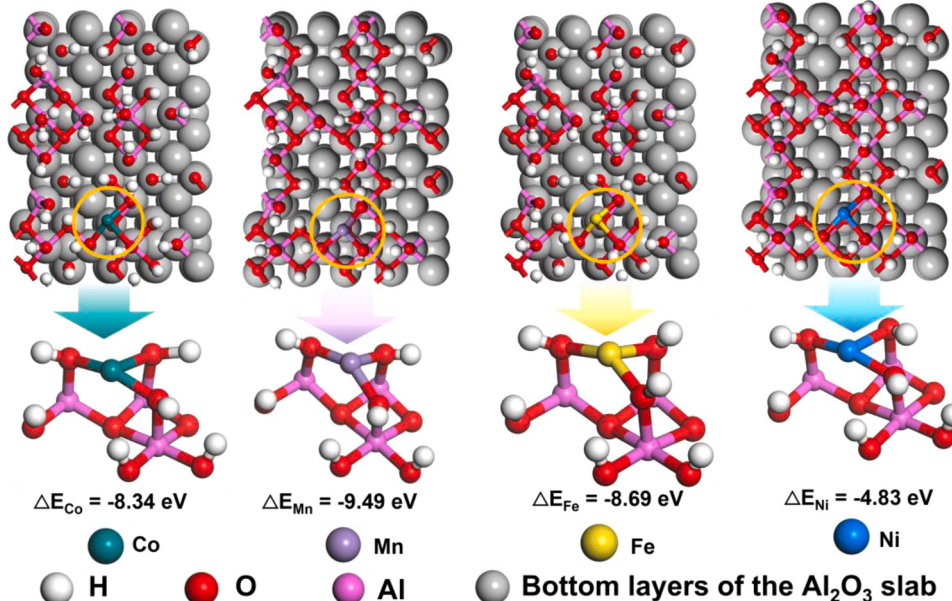
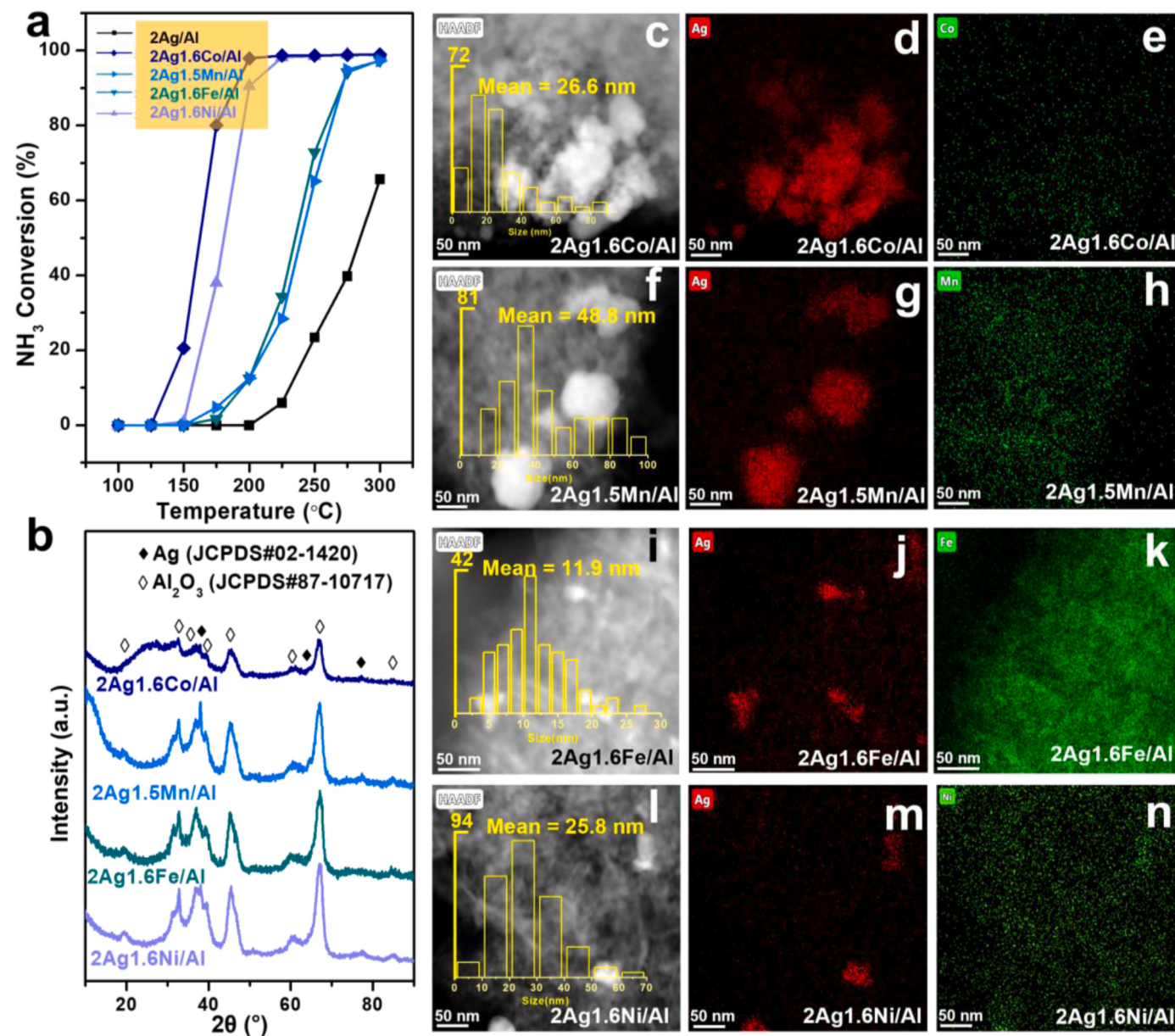


Fig. 5. DFT calculation results for the anchoring capability of Co, Mn, Fe, or Ni on the  $\gamma$ -Al<sub>2</sub>O<sub>3</sub> (100) surface.



**Fig. 6.** NH<sub>3</sub>-SCO performance tests and structural properties of 2Ag1.6Co/Al, 2Ag1.5Mn/Al, 2Ag1.6Fe/Al, and 2Ag1.6Ni/Al catalysts: (a) NH<sub>3</sub>-SCO test; (b) XRD patterns; HAADF-STEM images and EDS mapping of (c–e) 2Ag1.6Co/Al, (f–h) 2Ag1.5Mn/Al, (i–k) 2Ag1.6Fe/Al, (l–n) 2Ag1.6Ni/Al.

anchoring strengths on the hydroxyl groups on the Al<sub>2</sub>O<sub>3</sub> surface, which could affect the dispersion of Ag species to a certain extent, resulting in different NH<sub>3</sub>-SCO activities and N<sub>2</sub> selectivity.

#### 4. Conclusion

Based on the observation that Cu preferentially anchors on the surface hydroxyl groups of γ-Al<sub>2</sub>O<sub>3</sub> over Ag, we propose a 'pre-occupied-anchoring-site' strategy to construct more efficient NH<sub>3</sub>-SCO active sites. This strategy employed cheaper Cu to preferentially occupy the anchoring sites, inducing the aggregation of Ag. The low-loading Ag species were successfully aggregated into highly dispersed Ag<sub>NPs</sub> using a simple wet impregnation method. This approach reduced the catalyst cost to *ca.* one-fifth while ensuring consistent catalytic activity. When the Ag loading was 2 wt% and the Ag:Cu molar ratio was controlled at 2:3 (2Ag1.8Cu/Al), Ag atoms aggregated into Ag<sub>NPs</sub> on the γ-Al<sub>2</sub>O<sub>3</sub> surface due to the limited availability of anchoring sites, thus exhibiting excellent NH<sub>3</sub>-SCO activity similar to that of 10 wt% Ag/

Al<sub>2</sub>O<sub>3</sub> catalyst. The synergistic effect between the Cu and Ag components contributed to improved N<sub>2</sub> selectivity, H<sub>2</sub>O, SO<sub>2</sub> resistance, and catalytic stability. This "pre-occupied-anchoring-site" strategy has broad applicability to various inexpensive transition metals, such as Mn, Co, Ni, and Fe. These metals can preoccupy the Ag anchoring sites, forcing the more expensive Ag to agglomerate into Ag<sub>NPs</sub>. This cost-effective "pre-occupied-anchoring-site" mechanism offers a promising avenue for designing cheaper, more efficient, and stable nanoparticle materials for heterogeneous catalysis applications.

#### CRediT authorship contribution statement

F. W. conceived and supervised the project. Z. L. performed the experiments, DFT calculations and wrote the manuscript. S. X. assisted with the experiments. C. Z., P. N. and H. H. assisted with the interpretation of experimental results. F. L., K. L. and X. C. Z. directed the study and assisted with manuscript writing. All authors discussed the results and commented on the manuscript.

## Declaration of Competing Interest

The authors declare that they have no known competing financial interests or personal relationships that could have appeared to influence the work reported in this paper.

## Data Availability

Data will be made available on request.

## Acknowledgment

F. W. thanks the support from the National Natural Science Foundation of China (52370113, 52000093), and Yunnan Fundamental Research Projects (202101BE070001–001). F. L. acknowledges the Startup Fund from the University of Central Florida (UCF). S. X. thanks the support from the Preeminent Postdoctoral Program (P3) at UCF. This research used beamline 7-BM (QAS) of the National Synchrotron Light Source II, a U.S. Department of Energy (DOE) Office of Science User Facility operated for the DOE Office of Science by Brookhaven National Laboratory under Contract No. DE-SC0012704. X. C. Z. acknowledges the support by Hong Kong Global STEM Professorship Scheme.

## Appendix A. Supporting information

Supplementary data associated with this article can be found in the online version at [doi:10.1016/j.apcatb.2023.123655](https://doi.org/10.1016/j.apcatb.2023.123655).

## References

- [1] J. Tursic, A. Berner, B. Podkrajsek, I. Grgic, Influence of ammonia on sulfate formation under haze conditions, *Atmos. Environ.* 38 (2004) 2789–2795, <https://doi.org/10.1016/j.atmosenv.2004.02.036>.
- [2] B.W. Chu, X. Zhang, Y.C. Liu, H. He, Y. Sun, J.K. Jiang, J.H. Li, J.M. Hao, Synergetic formation of secondary inorganic and organic aerosol: effect of SO<sub>2</sub> and NH<sub>3</sub> on particle formation and growth, *Atmos. Chem. Phys.* 16 (2016) 14219–14230, <https://doi.org/10.5194/acp-16-14219-2016>.
- [3] I.M. Centeno, S. Castillo, G.A. Fuentes, Enhanced emissions of NH<sub>3</sub>, N<sub>2</sub>O and H<sub>2</sub> from a Pd-only TWC and supported Pd model catalysts: Light-off and sulfur level studies, *Appl. Catal. B.* 119–120 (2012) 234–240, <https://doi.org/10.1016/j.apcatb.2012.02.030>.
- [4] J.G.J. Olivier, A.F. Bouwman, K.W. Van der Hoek, J.J.M. Berdowski, Global air emission inventories for anthropogenic sources of NO<sub>x</sub>, NH<sub>3</sub> and N<sub>2</sub>O in 1990, *Environ. Pollut.* 102 (1998) 135–148, [https://doi.org/10.1016/S0269-7491\(98\)80026-2](https://doi.org/10.1016/S0269-7491(98)80026-2).
- [5] Y. Pan, S. Tian, D. Liu, Y. Fang, X. Zhu, Q. Zhang, B. Zheng, G. Michalski, Y. Wang, Reply to comment on 'fossil fuel combustion-related emissions dominate atmospheric ammonia sources during severe haze episodes: evidence from N-15-stable isotope in size-resolved aerosol ammonium', *Environ. Sci. Technol.* 50 (2016) 10767–10768, <https://doi.org/10.1021/acs.est.6b04197>.
- [6] Y. Inomata, S. Hata, M. Mino, E. Kiyonaga, K. Morita, K. Hikino, K. Yoshida, H. Kubota, T. Toyao, K. Shimizu, bulk vanadium oxide versus conventional V<sub>2</sub>O<sub>5</sub>/TiO<sub>2</sub>: NH<sub>3</sub>-SCR catalysts working at a low temperature below 150 °C, *ACS Catal.* 9 (2019) 9327–9331, <https://doi.org/10.1021/acscatal.9b02695>.
- [7] H. Wang, R. Zhang, Y. Liu, P. Li, H. Chen, Selective catalytic oxidation of ammonia over nano Cu/zeolites with different topologies, *Environ. Sci. Nano.* 7 (2020) 1399–1414, <https://doi.org/10.1039/d0en0007h>.
- [8] M.H.M.T. Assumpção, R.M. Piasentin, P. Hammer, R.F.B.D. Souza, G.S. Buzzo, M. Santos, E.V. Spinacé, A.O. Neto, J.C.M. Silva, Oxidation of ammonia using PtRh/C electrocatalysts: fuel cell and electrochemical evaluation, *Appl. Catal. B* 174 (2015) 136–144, <https://doi.org/10.1016/j.apcatb.2015.02.021>.
- [9] W. Chen, Y. Ma, Z. Qu, Q. Liu, W. Huang, X. Hu, N. Yan, Mechanism of the selective catalytic oxidation of slip ammonia over Ru-modified Ce-Zr complexes determined by in situ diffuse reflectance infrared fourier transform spectroscopy, *Environ. Sci. Technol.* 48 (2014) 12199–12205, <https://doi.org/10.1021/es502369f>.
- [10] X. Cui, L. Chen, Y. Wang, H. Chen, W. Zhao, Y. Li, J. Shi, Fabrication of hierarchically porous Ru<sub>2</sub>O<sub>3</sub>-CuO/Al<sub>2</sub>O<sub>3</sub> composite as highly efficient catalyst for ammonia-selective catalytic oxidation, *ACS Catal.* 4 (2014) 2195–2206, <https://doi.org/10.1021/cs500421x>.
- [11] X. Cui, J. Zhou, Z. Ye, H. Chen, L. Li, M. Ruan, J. Shi, Selective catalytic oxidation of ammonia to nitrogen over mesoporous CuO/RuO<sub>2</sub> synthesized by co-nanocasting-replication method, *J. Catal.* 270 (2010) 310–317, <https://doi.org/10.1016/j.jcat.2010.01.005>.
- [12] J. Fu, K. Yang, C. Ma, N. Zhang, H. Gai, Bimetallic Ru-Cu as a highly active, selective and stable catalyst for catalytic wet oxidation of aqueous ammonia to nitrogen, *Appl. Catal. B.* 184 (2016) 216–222, <https://doi.org/10.1016/j.apcatb.2015.11.031>.
- [13] J. Gong, R.A. Ojifinni, T.S. Kim, J.M. White, C.B. Mullins, Selective catalytic oxidation of ammonia to nitrogen on atomic oxygen precovered Au(111), *J. Am. Chem. Soc.* 128 (2006) 9012–9013, <https://doi.org/10.1021/ja062624w>.
- [14] Z. Wang, Z. Qu, R. Fan, The Al promotional effect for Ce<sub>0.4</sub>Zr<sub>0.6</sub>O<sub>2</sub> mixed oxides in selective catalytic oxidation of ammonia to nitrogen, *Sep. Purif. Technol.* 147 (2015) 24–31, <https://doi.org/10.1016/j.seppur.2015.04.006>.
- [15] M. Lin, B. An, N. Niimi, Role of the acid site for selective catalytic oxidation of NH<sub>3</sub> over Au/Nb<sub>2</sub>O<sub>5</sub>, *ACS Catal.* 9 (2019) 1753–1756, <https://doi.org/10.1021/acscatal.8b04272>.
- [16] F. Wang, Y. Zhu, Z. Li, Y. Shan, W. Shan, X. Shi, Y. Yu, Promoting effect of acid sites on NH<sub>3</sub>-SCO activity with water vapor participation for Pt-Fe/ZSM-5 catalyst, *Catal. Today* 36 (2020) 311–317, <https://doi.org/10.1016/j.cattod.2020.06.039>.
- [17] M. Lin, B. An, T. Takei, T. Shishido, T. Ishida, Features of Nb<sub>2</sub>O<sub>5</sub> as a metal oxide support of Pt and Pd catalysts for selective catalytic oxidation of NH<sub>3</sub> with high N<sub>2</sub> selectivity, *J. Catal.* 389 (2020) 366–374, <https://doi.org/10.1016/j.jcat.2020.05.040>.
- [18] H. Zhao, Z. Qu, H. Sun, Rational design of spinel CoMn<sub>2</sub>O<sub>4</sub> with Co-enriched surface as high-activity catalysts for NH<sub>3</sub>-SCO reaction, *Appl. Surf. Sci.* 529 (2020) 147044–147052, <https://doi.org/10.1016/j.apsusc.2020.147044>.
- [19] J. Guo, W. Yang, Y. Zhang, L. Gan, C. Fan, J. Chen, Y. Peng, J. Li, A multiple-active-site Cu/SSZ-13 for NH<sub>3</sub>-SCO: Influence of Si/Al ratio on the catalytic performance, *Catal. Commun.* 135 (2020) 105751, <https://doi.org/10.1016/j.catcom.2019.105751>.
- [20] C. Chen, Y. Cao, S. Liu, W. Jia, The effect of SO<sub>2</sub> on NH<sub>3</sub>-SCO and SCR properties over Cu/SCR catalyst, *Appl. Surf. Sci.* 507 (2020) 145153–145161, <https://doi.org/10.1016/j.apsusc.2019.145153>.
- [21] G. Jiang, F. Zhang, Z. Wei, Z. Wang, Y. Sun, Selective catalytic oxidation of ammonia over LaMAl<sub>11</sub>O<sub>19-δ</sub> (M = Fe, Cu, Co, and Mn) hexaaluminates catalysts at high temperatures in the Claus process, *Catal. Sci. Technol.* 10 (2020) 1477–1491, <https://doi.org/10.1039/c9cy02512j>.
- [22] Y. Zhang, X. Xia, B. Liu, S. Deng, D. Xie, Q. Liu, Y. Wang, J. Wu, X. Wang, J. Tu, Multiscale graphene-based materials for applications in sodium ion batteries, *Adv. Energy Mater.* 9 (2019) 1803342, <https://doi.org/10.1002/aenm.201803342>.
- [23] T. Zhang, H. Chang, Y. You, C. Shi, J. Li, Excellent activity and selectivity of one-pot synthesized Cu-SSZ-13 catalyst in the selective catalytic oxidation of ammonia to nitrogen, *Environ. Sci. Technol.* 52 (2018) 4802–4808, <https://doi.org/10.1021/acs.est.8b00267>.
- [24] W. Yue, R. Zhang, N. Liu, B. Chen, Selective catalytic oxidation of ammonia to nitrogen over orderly mesoporous CuFe<sub>2</sub>O<sub>4</sub> with high specific surface area, *Chin. Sci. Bull.* 59 (2014) 3980–3986, <https://doi.org/10.1007/s11434-014-0495-z>.
- [25] H. Wang, M. Lin, T. Murayama, S. Feng, M. Haruta, Ag size/structure-dependent effect on low-temperature selective catalytic oxidation of NH<sub>3</sub> over Ag/MnO<sub>2</sub>, *ACS Catal.* 11 (2021) 8576–8584, <https://doi.org/10.1021/acscatal.1c01130>.
- [26] M. Zhou, Z. Wang, Q. Sun, J. Wang, C. Zhang, D. Chen, X. Li, High-performance Ag-Cu nanoalloy catalyst for the selective catalytic oxidation of ammonia, *ACS Appl. Mater. Interfaces* 11 (2019) 46875–46885, <https://doi.org/10.1021/acsami.9b16349>.
- [27] L. Zhang, H. He, Mechanism of selective catalytic oxidation of ammonia to nitrogen over Ag/Al<sub>2</sub>O<sub>3</sub>, *J. Catal.* 268 (2009) 18–25, <https://doi.org/10.1016/j.jcat.2009.08.011>.
- [28] Z. Qu, H. Wang, S. Wang, H. Cheng, Y. Qin, Role of the support on the behavior of Ag-based catalysts for NH<sub>3</sub> selective catalytic oxidation (NH<sub>3</sub>-SCO), *Appl. Surf. Sci.* 316 (2014) 373–379, <https://doi.org/10.1016/j.apsusc.2014.08.023>.
- [29] F. Wang, G. He, B. Zhang, M. Chen, X. Chen, Insights into the activation effect of H<sub>2</sub> pretreatment on Ag/Al<sub>2</sub>O<sub>3</sub> catalyst for the selective oxidation of ammonia, *ACS Catal.* 9 (2019) 1437–1445, <https://doi.org/10.1021/acscatal.8b03744>.
- [30] F. Wang, J. Ma, G. He, M. Chen, S. Wang, Synergistic effect of TiO<sub>2</sub>-SiO<sub>2</sub> in Ag/Si-Ti catalyst for the selective catalytic oxidation of ammonia, *Ind. Eng. Chem. Res.* 52 (2018) 11903–11910, <https://doi.org/10.1021/acs.iecr.8b02205>.
- [31] F. Wang, J. Ma, G. He, M. Chen, C. Zhang, Nanosize effect of Al<sub>2</sub>O<sub>3</sub> in Ag/Al<sub>2</sub>O<sub>3</sub> catalyst for the selective catalytic oxidation of ammonia, *ACS Catal.* 8 (2018) 2670–2682, <https://doi.org/10.1021/acscatal.7b03799>.
- [32] F. Wang, Z. Li, H. Wang, M. Chen, C. Zhang, P. Ning, H. He, Nano-sized Ag rather than single-atom Ag determines CO oxidation activity and stability, *Nano Res.* 15 (2021) 452–456, <https://doi.org/10.1007/s12274-021-3501-1>.
- [33] M. Jabłońska, A.M. Beale, M. Nocuń, R. Palkovits, Ag-Cu based catalysts for the selective ammonia oxidation into nitrogen and water vapour, *Appl. Catal. B* 232 (2018) 275–287, <https://doi.org/10.1016/j.apcatb.2018.03.029>.
- [34] F. Wang, J. Ma, S. Xin, Q. Wang, J. Xu, C. Zhang, H. He, X. Zeng, Resolving the puzzle of single-atom silver dispersion on nanosized γ-Al<sub>2</sub>O<sub>3</sub> surface for high catalytic performance, *Nat. Commun.* 11 (2020) 529–538, <https://doi.org/10.1038/s41467-019-13937-1>.
- [35] J.P. Perdew, K. Burke, M. Ernzerhof, Generalized gradient approximation made Simple, *Phys. Rev. Lett.* 77 (1996) 3865–3868, <https://doi.org/10.1103/PhysRevLett.77.3865>.
- [36] S. Grimme, S. Ehrlich, L. Goerigk, Effect of the damping function in dispersion corrected density functional theory, *J. Comput. Chem.* 32 (2011) 1456–1465, <https://doi.org/10.1002/jcc.21759>.
- [37] G. Kresse, J. Furthmüller, Efficient iterative schemes for ab initio total-energy calculations using a plane-wave basis set, *Phys. Rev. B* 54 (1996) 11169–11186, <https://doi.org/10.1103/PhysRevB.54.11169>.
- [38] G. Kresse, D. Joubert, From ultrasoft pseudopotentials to the projector augmented-wave method, *Phys. Rev. B* 59 (1999) 1758–1775, <https://doi.org/10.1103/PhysRevB.59.1758>.

- [39] H. Deng, Y. Yu, H. He, Discerning the role of Ag–O–Al entities on Ag/ $\gamma$ -Al<sub>2</sub>O<sub>3</sub> surface in NO<sub>x</sub> selective reduction by ethanol, *J. Phys. Chem. C* 119 (2015) 3132–3142, <https://doi.org/10.1021/jp5114416>.
- [40] H. Deng, Y. Yu, H. He, Adsorption states of typical intermediates on Ag/Al<sub>2</sub>O<sub>3</sub> catalyst employed in the selective catalytic reduction of NO<sub>x</sub> by ethanol, *Chin. J. Catal.* 36 (2015) 1312–1320, [https://doi.org/10.1016/S1872-2067\(15\)60873-7](https://doi.org/10.1016/S1872-2067(15)60873-7).
- [41] J. Lu, J.J. Bravo-Suárez, M. Haruta, S.T. Oyama, Direct propylene epoxidation over modified Ag/CaCO<sub>3</sub> catalysts, *Appl. Catal. A* 302 (2006) 283–295, <https://doi.org/10.1016/j.apcata.2006.01.023>.
- [42] T.H. Ballinger, J.T.Y. Jr, IR spectroscopic detection of lewis acid sites on Al<sub>2</sub>O<sub>3</sub> using adsorbed CO correlation with Al-OH group removal, *Langmuir* 7 (1991) 3041–3045, <https://doi.org/10.1021/la00060a022>.
- [43] H. KnÖzinger, P. Ratnasamy, Catalytic aluminas: surface models and characterization of surface sites, *Catal. Rev. Sci. Eng.* 17 (2007) 31–70, <https://doi.org/10.1080/03602457808080878>.
- [44] M. Cornac, A. Janin, J.C. Lavallee, Application of FTIR spectroscopy to the study of sulfidation of Mo catalysts supported on alumina or silica (4000–400 cm<sup>-1</sup> range), *Infrared Phys. Chem.* 24 (1984) 143–150, [https://doi.org/10.1016/0020-0891\(84\)90062-9](https://doi.org/10.1016/0020-0891(84)90062-9).
- [45] M.I. Zaki, H. KnÖzinger, Carbon monoxide-A low temperature infrared probe for the characterization of hydroxyl group properties on metal oxide surfaces, *Mater. Chem. Phys.* 17 (1987) 201–215, [https://doi.org/10.1016/0254-0584\(87\)90056-3](https://doi.org/10.1016/0254-0584(87)90056-3).
- [46] G.W. Wagner, L.R. Procell, R.J. O'Connor, S. Munavalli, K.J. Klabunde, Reactions of VX, GB, GD, and HD with nanosize Al<sub>2</sub>O<sub>3</sub>. Formation of aluminophosphonates, *J. Am. Chem. Soc.* 123 (2001) 1636–1644, <https://doi.org/10.1021/ja003518b>.
- [47] E.C. Decanio, J.C. Edwards, J.W. Bruno, Solid-State <sup>1</sup>H MAS NMR characterization of  $\gamma$ -alumina and modified  $\gamma$ -aluminas, *J. Catal.* 148 (1994) 76–83, <https://doi.org/10.1006/jcat.1994.1187>.
- [48] P. Nortier, P. Fourre, A. Saad, O. Saur, J.C. Lavallee, Effects of crystallinity and morphology on the surface properties of alumina, *Appl. Catal. A* 61 (1990) 141–160, [https://doi.org/10.1016/S0166-9834\(00\)82140-5](https://doi.org/10.1016/S0166-9834(00)82140-5).
- [49] T.H. Ballinger, J.T. Yates, IR spectroscopic detection of Lewis acid sites on alumina using adsorbed carbon monoxide. Correlation with Al<sub>2</sub>O<sub>3</sub>-hydroxyl group removal, *Langmuir* 7 (2002) 3041–3045, <https://doi.org/10.1021/la00060a022>.
- [50] C. Choong, Z. Zhong, H. Lin, W. Zhan, T.P. Ang, A. Borgna, J. Lin, H. Liang, L. Chen, Effect of calcium addition on catalytic ethanol steam reforming of Ni/Al<sub>2</sub>O<sub>3</sub>: I. Catalytic stability, electronic properties and coking mechanism, *Appl. Catal. A* 407 (2011) 145–154, <https://doi.org/10.1016/j.apcata.2011.08.037>.
- [51] R.L. Puurunen, M. Lindblad, A. Root, I.K. Outi, A. Successive reactions of gaseous trimethylaluminium and ammonia on porous alumina, *Phys. Chem. Chem. Phys.* 3 (2001) 1093–1102, <https://doi.org/10.1039/B0072490>.
- [52] M. Digne, P. Sautet, P. Raybaud, P. Euzen, H. Toulhoat, Hydroxyl groups on  $\gamma$ -alumina surfaces: a DFT study, *J. Catal.* 211 (2002) 1–5, <https://doi.org/10.1006/jcat.2002.3741>.
- [53] M. Newville, IFEFFIT: interactive XAFS analysis and FEFF fitting, *J. Synchrotron Radiat.* 8 (2010) 322–324, <https://doi.org/10.1107/S0909049500016964>.
- [54] J. Shibata, K.I. Shimizu, Y. Takada, A. Shichi, T. Hattori, Structure of active Ag clusters in Ag zeolites for SCR of NO by propane in the presence of hydrogen, *J. Catal.* 227 (2004) 367–374, <https://doi.org/10.1016/j.jcat.2004.08.007>.
- [55] K.A. Bethke, H.H. Kung, Supported Ag catalysts for the lean reduction of NO with C<sub>3</sub>H<sub>6</sub>, *J. Catal.* 172 (1997) 93–102, <https://doi.org/10.1006/jcat.1997.1794>.
- [56] K. Shimizu, J. Shibata, H. Yoshida, A. Hattori, Silver-alumina catalysts for selective reduction of NO by higher hydrocarbons: structure of active sites and reaction mechanism, *Appl. Catal. B* 30 (2001), [https://doi.org/10.1016/S0926-3373\(00\)00229-0](https://doi.org/10.1016/S0926-3373(00)00229-0).
- [57] O.I. Gromov, E.M. Zubanova, E.N. Golubeva, V.F. Plyusnin, G.M. Zhidomirov, M.Y. Melnikov, UV-Vis identification and DFT-assisted prediction of structures of Cu(II)-alkyl chlorocomplexes, *J. Phys. Chem. A* 116 (2012) 11581–11585, <https://doi.org/10.1021/jp309222y>.
- [58] N. Riaz, F.K. Chong, B.K. Dutta, Z.B. Man, M.S. Khan, E. Nurlaela, Photodegradation of Orange II under visible light using Cu-Ni/TiO<sub>2</sub>: Effect of calcination temperature, *Chem. Eng. J.* 185–186 (2012) 108–119, <https://doi.org/10.1016/j.cej.2012.01.052>.
- [59] A. Sandoval, A. Aguilar, C. Louis, A. Traverse, R. Zanella, Bimetallic Au-Ag/TiO<sub>2</sub> catalyst prepared by deposition-precipitation: high activity and stability in CO oxidation, *J. Catal.* 281 (2011) 40–49, <https://doi.org/10.1016/j.jcat.2011.04.003>.
- [60] Y. Nagai, T. Hirabayashi, K. Dohmae, N. Takagi, T. Minami, H. Shinjoh, S. I. Matsumoto, Sintering inhibition mechanism of platinum supported on ceria-based oxide and Pt-oxide-support interaction, *J. Catal.* 242 (2006) 103–109, <https://doi.org/10.1016/j.jcat.2006.06.002>.
- [61] P. Verma, K. Yuan, Y. Kuwahara, K. Mori, H. Yamashita, Enhancement of plasmonic activity by Pt/Ag bimetallic nanocatalyst supported on mesoporous silica in the hydrogen production from hydrogen storage material, *Appl. Catal. B* 223 (2018) 10–15, <https://doi.org/10.1016/j.apcatab.2017.05.017>.
- [62] D. Jiang, G. Wan, C.E. García-Vargas, L. Li, X.I. Pereira-Hernández, C. Wang, Y. Wang, Elucidation of the active sites in single-atom Pd<sub>1</sub>/CeO<sub>2</sub> Catalysts for low-temperature CO oxidation, *ACS Catal.* 10 (2020) 11356–11364, <https://doi.org/10.1021/acscatal.Oc02480>.
- [63] J. Pei, B. Peng, H. Lin, W. Chen, Y. Wang, J. Dong, J. Mao, D. Jia, W. Zhu, Z. Zhuang, Single-atom Ru on Al<sub>2</sub>O<sub>3</sub> for highly active and selective 1,2-Dichloroethane catalytic degradation, *ACS Appl. Mater. Interfaces* 13 (2021) 53683–53690, <https://doi.org/10.1021/acsami.1c08471>.
- [64] C. Wang, S. Mao, Z. Wang, Y. Chen, W. Yuan, Y. Ou, H. Zhang, Y. Gong, Y. Wang, B. Mei, Z. Jiang, Y. Wang, Insight into single-atom-induced unconventional size dependence over CeO<sub>2</sub>-supported Pt catalysts, *Chem* 6 (2020) 752–765, <https://doi.org/10.1016/j.chempr.2019.12.029>.
- [65] Wei Zhou, Ting Li, Jianqiang Wang, Yang Qu, Kai Pan, Composites of small Ag clusters confined in the channels of well-ordered mesoporous anatase TiO<sub>2</sub> and their excellent solar-light-driven photocatalytic performance, *Nano Res.* 5 (2014) 731–742, <https://doi.org/10.1007/s12274-014-0434-y>.
- [66] Q. An, G. Xu, J. Liu, Y. Wang, Y. Yu, H. He, Designing a bifunctional Pt/Cu-SZS-13 catalyst for ammonia-selective catalytic oxidation with superior selectivity, *ACS Catal.* (2023) 6851–6861, <https://doi.org/10.1021/acscatal.3c01322>.
- [67] L. Gang, B.G. Anderson, J. van Grondelle, R.A. van Santen, Low temperature selective oxidation of ammonia to nitrogen on silver-based catalysts, *Appl. Catal. B* 40 (2003) 101–110, [https://doi.org/10.1016/S0926-3373\(02\)00129-7](https://doi.org/10.1016/S0926-3373(02)00129-7).
- [68] P.H. McBreen, M. Moskovits, A surface-enhanced Raman study of ethylene and oxygen interacting with supported silver catalysts, *J. Catal.* 103 (1987) 188–199, [https://doi.org/10.1002/1-9517\(87\)90105-9](https://doi.org/10.1002/1-9517(87)90105-9).
- [69] J. Rodriguez, Metal-metal bonding on surfaces: electronic and chemical properties of Ag on Ru(001), *Surf. Sci.* 296 (1993) 149–163, [https://doi.org/10.1016/0039-6028\(93\)91143-D](https://doi.org/10.1016/0039-6028(93)91143-D).
- [70] M. Jabłońska, K. Nothdurft, M. Nocuń, V. Girman, R. Palkovits, Redox-performance correlations in Ag-Cu-Mg-Al, Ce-Cu-Mg-Al, and Ga-Cu-Mg-Al hydrotalcite derived mixed metal oxides, *Appl. Catal. B* 207 (2017) 385–396, <https://doi.org/10.1016/j.apcatab.2017.01.079>.
- [71] Z. Li, J. Zhao, J. Gao, Y. Li, S. Bao, K. Li, P. Ning, F. Wang, “Reduction-aggregation” strategy to construct a low-cost and high-efficiency Ag/Al<sub>2</sub>O<sub>3</sub> catalyst for NH<sub>3</sub>-SCO, *Sep. Purif. Technol.* 317 (2023) 123881, <https://doi.org/10.1016/j.seppur.2023.123881>.
- [72] D. Ma, Y. Ying, K. Zhang, Y. Gao, L. Zhou, A. Song, Y. Zhu, K. Xie, T. Jin, H. Huang, Greatly enhanced CO<sub>2</sub> electrocatalytic reduction performance of Ag<sub>2</sub>Se nanocatalyst via phase-engineering, *Appl. Catal. B* 316 (2022) 121658, <https://doi.org/10.1016/j.apcatab.2022.121658>.
- [73] J. Li, T. Shi, F. Tian, S. Liu, Q. Fan, Y. Wu, M. Sun, H. Zhang, Y. Lei, F. Liu, S. Zeng, Elucidating reaction pathways in CO<sub>2</sub> electroreduction: case study of Ag and Cu<sub>2</sub>O@Ag catalysts, *J. Catal.* 417 (2023) 1–13, <https://doi.org/10.1016/j.jcat.2022.11.035>.
- [74] Z. Wang, Q. Sun, D. Wang, Z. Hong, Z. Qu, Hollow ZSM-5 zeolite encapsulated Ag nanoparticles for SO<sub>2</sub>-resistant selective catalytic oxidation of ammonia to nitrogen, *Sep. Purif. Technol.* 209 (2019) 1016–1026, <https://doi.org/10.1016/j.seppur.2018.09.045>.
- [75] M. Jabłońska, R. Palkovits, Copper based catalysts for the selective ammonia oxidation into nitrogen and water vapour-recent trends and open challenges, *Appl. Catal. B* 181 (2016) 332–351, <https://doi.org/10.1016/j.apcatab.2015.07.017>.
- [76] C. Chen, Y. Cao, S. Liu, J. Chen, W. Jia, The catalytic properties of Cu modified attapulgite for NH<sub>3</sub>-SCO and NH<sub>3</sub>-SCR reactions, *Appl. Surf. Sci.* 480 (2019) 537–547, <https://doi.org/10.1016/j.apsusc.2019.03.024>.
- [77] Z. Wang, Z. Qu, X. Quan, Z. Li, H. Wang, Selective catalytic oxidation of ammonia to nitrogen over CuO-CeO<sub>2</sub> mixed oxides prepared by surfactant-templated method, *Appl. Catal. B* 134–135 (2013) 153–166, <https://doi.org/10.1016/j.apcatab.2013.01.029>.
- [78] Z. Qu, Z. Wang, X. Zhang, H. Wang, Role of different coordinated Cu and reactive oxygen species on the highly active Cu-Ce-Zr mixed oxides in NH<sub>3</sub>-SCO: a combined in situ EPR and O<sub>2</sub>-TPD approach, *Catal. Sci. Technol.* 6 (2016) 4491–4502, <https://doi.org/10.1039/C5CY02125A>.